

# Characterization and evolution of seismic sequences in the normal fault environment of the Southern Apennines

Francesco Scotto di Uccio<sup>1</sup>, Maddalena Michele<sup>2</sup>, Claudio Strumia<sup>3</sup>, Mariano Supino<sup>2</sup>, Gregory C. Beroza<sup>4</sup>, Lauro Chiaraluce<sup>2</sup>, Nicola D'Agostino<sup>2</sup>, and Gaetano Festa<sup>1</sup>

<sup>1</sup>Università di Napoli Federico II

<sup>2</sup>Istituto Nazionale di Geofisica e Vulcanologia

<sup>3</sup>University of Naples Federico II

<sup>4</sup>Stanford University

January 15, 2024

## Abstract

The use of seismic catalogs enhanced through advanced detection techniques improves the understanding of earthquake processes by illuminating the geometry and mechanics of fault systems. In this study, we performed accurate hypocentral locations, source parameters estimation and stress release modelling from deep catalogs of microseismic sequences nucleating in the complex normal fault system of the Southern Apennines (Italy). The application of advanced location techniques resulted in the relocation of ~ 30% of the earthquakes in the enhanced catalogs, with relocated hypocenters clearly identifying local patches on kilometer-scale structures that feature consistent orientation with the main faults of the area. When mapping the stress change on the fault plane, the inter-event distance compared to the size of the events suggests that the dominant triggering mechanism within the sequences is static stress transfer. The distribution of events is not isotropic but dominantly aligned along the dip direction. These slip-dominated lineations could be associated with striations related to fault roughness and could map the boundary between locked and creeping domains in Apulian platform and basement.

# 1 **Characterization and evolution of seismic sequences in the normal** 2 **fault environment of the Southern Apennines**

3  
4 *Francesco Scotto di Uccio*<sup>1</sup>, *Maddalena Michele*<sup>2</sup>, *Claudio Strumia*<sup>1</sup>, *Mariano Supino*<sup>2</sup>,  
5 *Gregory C. Beroza*<sup>3</sup>, *Lauro Chiaraluce*<sup>2</sup>, *Nicola D'Agostino*<sup>2</sup>, *Gaetano Festa*<sup>1,2</sup>

6  
7 <sup>1</sup> Department of Physics 'Ettore Pancini', University of Napoli Federico II, 80126 Napoli, Italy.

8 <sup>2</sup> Istituto Nazionale di Geofisica e Vulcanologia, Rome, Italy.

9 <sup>3</sup> Department of Geophysics, Stanford University, Stanford, CA 94305, USA.

10  
11  
12 Corresponding author: Francesco Scotto di Uccio ([francesco.scottodiuccio@unina.it](mailto:francesco.scottodiuccio@unina.it))

## 13 14 15 **Key Points:**

- 16 • Accurate earthquake location for enhanced catalogs unveils kilometeric scale structures  
17 where seismic sequences occur in Southern Apennines.
- 18 • Static stress transfer drives the evolution of these seismic sequences, with earthquakes  
19 dominantly distributed along the dip direction.
- 20 • Slip-dominated alignments of the seismicity could map the fault roughness or the boundary  
21 between locked and creeping domains.  
22

## 23 **Abstract**

24 The use of seismic catalogs enhanced through advanced detection techniques improves the  
25 understanding of earthquake processes by illuminating the geometry and mechanics of fault  
26 systems. In this study, we performed accurate hypocentral locations, source parameters estimation  
27 and stress release modelling from deep catalogs of microseismic sequences nucleating in the  
28 complex normal fault system of the Southern Apennines (Italy). The application of advanced  
29 location techniques resulted in the relocation of ~30% of the earthquakes in the enhanced catalogs,  
30 with relocated hypocenters clearly identifying local patches on kilometer-scale structures that  
31 feature consistent orientation with the main faults of the area. When mapping the stress change on  
32 the fault plane, the inter-event distance compared to the size of the events suggests that the  
33 dominant triggering mechanism within the sequences is static stress transfer. The distribution of  
34 events is not isotropic but dominantly aligned along the dip direction. These slip-dominated  
35 lineations could be associated with striations related to fault roughness and could map the  
36 boundary between locked and creeping domains in Apulian platform and basement.

## 37 **Plain Language Summary**

38 The development of earthquake detection techniques, based on machine learning or similarity, has  
39 allowed to increase seismic catalogs of more than one order of magnitude. However, how much  
40 information can be extracted from these small cracklings is still to be understood, especially in  
41 complex normal fault systems, such as the Apennine environment in Italy. For seismic sequences  
42 in Southern Apennines, we show that only a few portion (about 30%) of events in enhanced  
43 catalogs can be further characterized in terms of location and source properties. Nevertheless, the  
44 use of deep catalogs allows to illuminate kilometric scale structures at depths between 8 and 15  
45 km, to define mechanisms for seismicity evolution, mainly driven by static stress triggering, to  
46 identify seismicity alignments along the slip direction, eventually associated with fault roughness  
47 or delimiting boundaries between locked and creeping regions.

## 48 **1 Introduction**

49 Seismic sequences are comprised of earthquakes that are clustered in space and time and that occur  
50 at a higher rate than the background seismicity. They contain powerful information for  
51 investigating the geometry and mechanical state of faults that may generate large magnitude

52 earthquakes. In the case of a major event, accurate location of foreshocks and aftershocks can  
53 inform the rupture process from the preparation phase to the arrest by illuminating the structural  
54 complexity of the causative fault (e.g., Lomax 2020, Waldhauser et al. 2021). Most sequences,  
55 however, occur during the interseismic period between large earthquakes, at smaller space scales,  
56 and feature main events of low to moderate magnitude (Chiaraluce et al. 2009). These sequences  
57 can last from few days (Stabile et al. 2012, Scotto di Uccio et al. 2023) to months or years (Kaviris  
58 et al. 2021) and can provide insights into stress conditions at depth, potential asperities (Festa et  
59 al. 2021), fluid diffusion (Chen et al. 2012), aseismic processes (Gualandi et al. 2017), or other  
60 forcing mechanisms that can perturb the stress state in the brittle crust (Silverii et al., 2019).

61 Knowledge of structures and processes from the analysis of the sequences strongly depends on the  
62 content and the magnitude of completeness of available catalogs. Recently, enhanced catalogs  
63 obtained through advanced automatic detection techniques such as machine learning and  
64 similarity-based approaches (Chamberlain et al. 2018, Zhu & Beroza 2018, Mousavi et al. 2020,  
65 Liu et al. 2020, Spallarossa et al. 2021, Scotto di Uccio et al. 2023, Sukan et al. 2023) have  
66 contributed to increase the number of newly cataloged events by more than one order of magnitude,  
67 improving the magnitude of completeness by at least one magnitude unit. Machine learning based  
68 phase pickers have been shown to provide phase arrival times consistent with analyst  
69 identifications (Mousavi et al. 2020, Cianetti et al. 2021, Münchmeyer et al. 2022), even for  
70 earthquakes outside the regions used in the training datasets (e.g., Mousavi et al. 2020, Park et al.  
71 2020, Tan et al. 2021). Furthermore, event similarity can be exploited for closely spaced events  
72 using cross-correlation to measure P and S arrivals for smaller magnitude earthquakes from  
73 template events (Poupinet et al. 1984, Vuan et al. 2018, Chamberlain et al. 2018).

74 Phase picks can be used for precise earthquake location using differential location methods  
75 (Waldhauser & Ellsworth 2000, Trugman & Shearer 2017). However, hypocenter determination  
76 of low magnitude earthquakes in enhanced catalogs is challenging because these events typically  
77 emerge from the noise only at the few closest stations with uncertain arrival times. A typical  
78 percentage of template matched events that can be relatively located from enhanced catalogs is ~  
79 20% (Cabrera et al. 2022). Nevertheless, accurate locations from deep catalogs can provide a high-  
80 resolution image of fault structures, help to discern their interaction (e.g., Ross et al. 2019, Park et  
81 al. 2022, Sukan et al. 2023), and illuminate paths for possible fluid migration (Ross et al. 2020,  
82 Vuan et al. 2020).

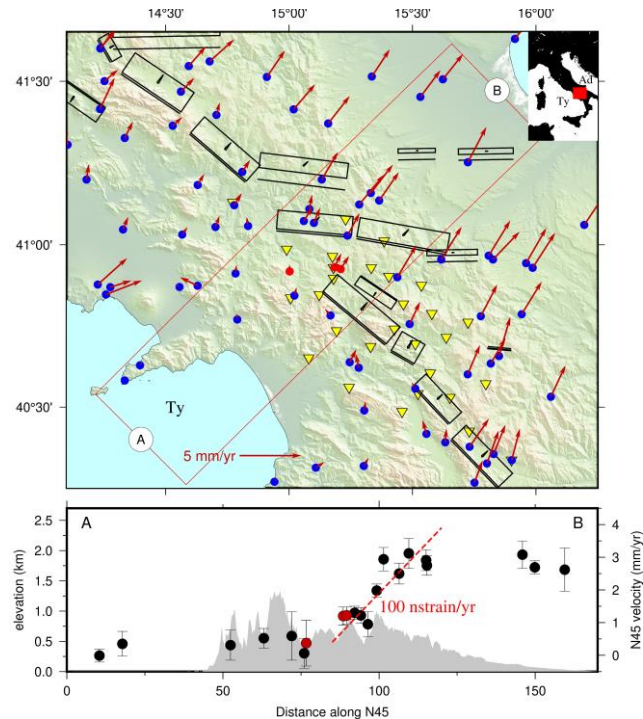
83 Deep catalogs can be statistically exploited in their space-time-magnitude evolution for inferring  
84 macroscopic physical processes to relate seismic sequences to background seismicity (Hermann  
85 et al. 2022, Scotto di Uccio et al. 2023), which may improve the predictability of short-term  
86 forecasting (Gulia & Wiemer 2019, Beroza et al. 2021). Reliable estimation of the frequency-  
87 magnitude characteristics of the catalogs requires a correct estimation of the event size and the  
88 catalog magnitude of completeness to avoid biases in b-value estimates (Marzocchi et al. 2020,  
89 Mancini et al. 2022).

90 Extracting physical constraints on the source process of events in deep catalogs is challenging due  
91 to the small signal-to-noise ratio and the narrow available frequency band. Local and moment  
92 magnitudes for small events can be estimated using time or frequency domain measurements (e.g.,  
93 Abercrombie 1995, Edwards et al. 2015, Hawthorne & Burtlow 2018, Supino et al. 2020, Scotto  
94 di Uccio et al. 2023). The source corner frequency (or event duration in time domain), which is a  
95 proxy for the earthquake size, can be obscured by anelastic attenuation effects (Deichmann, 2017)  
96 or the sampling rate (Abercrombie 2015). Several approaches have been proposed to reduce the  
97 correlation between the attenuation of the medium crossed by seismic waves and the source  
98 parameters. These are either based on the Empirical Green's function (EGFs) approach (Mori &  
99 Frankel 1990, Prieto et al. 2004), or based on the determination of attenuation relationships (Oth  
100 et al. 2007), which can allow a decrease in the minimum magnitude for which the source  
101 parameters can be estimated (Abercrombie 2015). While the use of EGFs is appealing in removing  
102 the propagation contribution, small events should be at least one point of magnitude smaller than  
103 the earthquake for most EGF approaches (Abercrombie & Rice 2005). EGF availability is often  
104 limited at the stations closest to the hypocenter, in a limited frequency band, where the signal  
105 emerges from the noise. When properly retrieving the source parameters for events in the sequence,  
106 they can help constrain the mechanisms associated with their evolution, e.g., whether they are  
107 triggered by stress release in cascade-like models or are driven by other forcing mechanisms (e.g.,  
108 Stabile et al. 2012, Yoon et al. 2019).

109 In this study we focused on seismic sequences in the Irpinia region, Southern Apennines (Italy).  
110 The area is one of the highest hazard regions of Italy (Stucchi et al. 2011) and experienced the  
111 most destructive seismic event in recent decades in that country. The 1980, M 6.9, Irpinia  
112 earthquake occurred on multiple, separate fault segments that were activated within 40s of the  
113 event origin (Figure 1), leading to more than 3000 casualties (Rovida et al. 2019). The region is

114 currently deforming, with a strain rate of  $\sim 100$  nstrain/yr corresponding to an increase of  $\sim 3$  mm/yr  
115 over 30 km across the axis of the Apennines (Daout et al., 2003; Figure 1). In the last 15 years, the  
116 area has been monitored by the Irpinia Near-Fault Observatory (INFO, triangles in Figure 1), with  
117 a dense seismic network of 31 stations equipped with accelerometers and short-period or broad-  
118 band seismometers (Iannaccone et al. 2010, Chiaraluce et al. 2022). Recent seismicity is  
119 characterized by low magnitude events (maximum magnitude 3.8), mainly occurring at depths  
120 between 8 and 15 km (De Landro et al. 2015), within the fault system that generated the 1980  
121 Irpinia earthquake and is mainly concentrated in a volume of low vs, high  $Q_p$ , high  $v_p/v_s$ , which  
122 suggests fluid-saturated conditions (Vassallo et al. 2016, Amoroso et al. 2017). Also, source  
123 parameters show a variability in the stress drop that could be modulated by fluid composition and  
124 concentration (Picozzi et al. 2021). In the area seismicity sometimes occurs clustered in seismic  
125 sequences that last several days, characterized by main events of magnitude lower than 3.5.  
126 Detailed studies of two sequences have shown a complex pattern for the seismicity and suggested  
127 that stress triggering can be the main driver of their evolution (Stabile et al. 2012, Festa et al.  
128 2021). Recently an enhanced catalog for 10 seismic sequences has been obtained for the area  
129 (Scotto di Uccio et al. 2023), built on the integration of machine learning and template matching,  
130 that increased the number of events relative to the existing manual catalog by a factor 7. In this  
131 study we seek to exploit the improved catalog to better understand the space-time evolution of the  
132 seismic sequences. We found that seismic sequences can be accurately located with uncertainties  
133 of  $\sim 100$  m, they occur on secondary structures with respect to the main segments of the 1980  
134 Irpinia earthquakes and their evolution appears to be mainly driven by static stress transfer.  
135 Preferential alignments of the seismicity along the dip direction might be an indication of  
136 simultaneous aseismic transients, especially for the most populated sequence.

137 First, we present the data used in the work (Section 2). Then, we describe the methods for  
138 accurately locating the events in the sequence, determining the source parameters and building a  
139 model to describe the stress release on the fault plane hosting the sequence (Section 3). Finally, we  
140 present the results obtained for the sequences, interpreting their spatio-temporal evolution (Section  
141 4), along with discussions and conclusions.



142 *Figure 1) Top panel: GPS velocity field in a Tyrrhenian reference frame. Yellow triangles indicate the seismic stations*  
 143 *of INFO. GPS stations SNAL, ANG1, and MTMR are displayed in red circles. The black boxes are the historical faults*  
 144 *that generated the largest earthquakes in the area, as reported by the Database of Individual Seismogenic Sources*  
 145 *(DISS, <https://seismofaults.eu/services/diss-services>). Bottom panel: Elevation along the A-B section of top panel and*  
 146 *velocity field related to the GPS stations within the red box of top panel along the N45E direction. The study area is*  
 147 *currently accumulating strain at  $\sim 100$  nstrain/yr corresponding to an increase of  $\sim 3$  mm/yr across the axial part of*  
 148 *the Apennines.*

## 149 **2 Data**

150 In this work we characterized the spatio-temporal evolution of seismic sequences that occurred  
 151 near the Irpinia Near Fault Observatory. The sequences occurred between 2011 and 2020 and  
 152 featured main events of low to moderate local magnitude ( $1.8 < M_l < 3.7$ ). We selected the  
 153 enhanced catalogs obtained by Scotto di Uccio et al. (2023) using machine learning derived  
 154 detections (EQTransformer, Mousavi et al. 2020) as template sets for a further similarity-based  
 155 detection (EQCorrscan, Chamberlain et al. 2018). The integration of machine learning and  
 156 template matching has been shown to improve the manual catalogs by a factor  $\sim 7$  in this region.  
 157 The catalogs for the sequences obtained in Scotto di Uccio et al. (2023) feature an improved  
 158 magnitude of completeness of more than one magnitude unit and provide  $\sim 1.8$ k events, with nearly  
 159 800 events in the Rocca San Felice sequence.

160 We extended the initial phase-pick dataset to all the stations not included in the detection step in  
161 Scotto di Uccio et al. (2023). We used the velocity data when available, and the acceleration data  
162 as a second choice, following the same strategy used in Scotto di Uccio et al. (2023).

163 The cross-correlation delay times for double difference earthquake re-locations were evaluated on  
164 traces decimated to 100 Hz (Michele et al., 2020), obtained trimming raw continuous waveforms  
165 around the origin time from absolute locations. In the evaluation of source parameters for the  
166 relocated events, we pre-processed the raw traces by removing the instrumental response,  
167 including a 5% Hann taper and a water level regularization during the deconvolution stage. We  
168 bracketed the *S* wave window from 1 s before to 3 s after the phase arrival time. We considered  
169 the frequency band that satisfied the condition of SNR between the event and the noise spectra  
170 larger than 3.5 based on a comparison with a 4s time window before the event origin time.

## 171 **3 Methods**

### 172 **3.1 Absolute and relative locations**

173 For locating the earthquakes in the enhanced catalogs, we used available P and S arrival times. For  
174 template events, we obtained phase arrival times with the machine learning picker. The consistency  
175 between the automatic and manual picks was demonstrated in Scotto di Uccio et al. (2023), who  
176 found that the residuals featured zero mean values and a slightly larger dispersion for the S phase  
177 (standard deviation of 0.2 s). For the low magnitude events identified by the template matching,  
178 they performed cross-correlation (CC) picking and retained those measurements with a CC value  
179 of greater than 0.7. The consistency of template picks helps to ensure the reliability of the CC-  
180 derived phase arrival times. Moreover, the similarity-based detection step can add missed picks by  
181 machine learning picker, also for events with moderate signal-to-noise ratio (Park et al. 2023).  
182 When an arrival time was declared by both pickers, we selected the phase provided by the machine  
183 learning technique. Arrival time uncertainties are estimated by considering the associated  
184 probability for machine learning picks and the CC values for template matching phases,  
185 respectively. We converted the probability values (ranging between 0.1 and 1.0) into discrete  
186 weights for location (from 0 to 4, increasing numbers correspond to larger uncertainties) according  
187 to the table proposed by Mousavi et al. (2020). For the template matching picks, we imposed at  
188 least the same level of accuracy of the machine learning picks used for the declaration, eventually

189 increasing the discrete weights for low cross-correlation values. We raised the discrete weights by  
190 one point for every decimal of CC coefficient detaching from 1.0.

191 We estimated earthquake location using NonLinLoc (Lomax et al. 2000), which adopts a  
192 probabilistic approach to determine the location using the travel time residuals with statistically  
193 robust uncertainties. We tested three velocity models for the location procedure. Starting from a 1-  
194 D layered velocity model tailored for the Irpinia area (Matrullo et al. 2013), we derived two  
195 gradient models, which smooth the discontinuities in the wave velocity across layer boundaries,  
196 by linearly interpolating values between either the top or the middle points of the layers (Figure  
197 S1). We note that the velocity model obtained fixing the velocity value at the top of the layers  
198 systematically overestimates the velocity in each layer. The interpolated model obtained by fixing  
199 the velocity values at the centre of the layers resulted in lower location uncertainties, so we selected  
200 this model for event location. A few poorly constrained events result in an unreliable shallow  
201 location estimate; for these cases, we selected the location solutions obtained from the expected  
202 values of the probability density function (Lomax et al. 2000).

203 We used absolute locations as the starting point for relative re-locations of events in each sequence  
204 using HYPODD (Waldhauser & Ellsworth 2000), based on differential travel times for event pairs.  
205 For the evaluation of the catalog delay times in each sequence we used the picks for event pairs  
206 separated by less than 10 km in absolute location at all the available stations. For CC differential  
207 travel times, we evaluated the delay times for events that were separated by less than 10 km, on  
208 seismograms decimated to 100 Hz and filtered in the frequency band [1.5 – 15] Hz (Schaff et al.  
209 2004, Michele et al. 2020).

210 We assessed the length of the time windows for extracting the waveforms around the P and S  
211 arrival times by performing parametric tests. Too short windows resulted into too high values of  
212 CC coefficients such that the reliability of the lag measurement was overestimated. We selected a  
213 1.1 s (1.4 s) long window around the P (S) phase arrival time for calculating the CC coefficients,  
214 imposing a maximum lag of 1s. We only retained delay times for events with CC coefficient higher  
215 than 0.7.

216 We estimated relative locations with HYPODD using an iterative least square procedure (LSQR)  
217 that minimized the differential time residuals for pairs of earthquakes recorded at common stations  
218 by adjusting the vector connecting their hypocentres (Waldhauser & Ellsworth 2000). We used 4

219 steps of 4 iterations (a total of 16 iterations) of damped and dynamically weighted least square  
 220 inversions. In the initial settings, we assigned higher weights to catalog delay times, for better  
 221 constraining the location of the clusters, and we increased the contribution of the CC differential  
 222 travel times in the following settings, to consider the different position of the events within the  
 223 cluster. The damping factor was selected to stabilize the problem (Waldhauser 2001). To avoid  
 224 inconsistency with ray patterns used in the absolute locations, we extracted a 1-D model composed  
 225 of 20 thin layers from a resampling of the velocity model used in the absolute locations.

226 LSQR only approximates some aspects of the uncertainty (Waldhauser & Ellsworth 2000), so we  
 227 applied the Singular Value Decomposition (SVD) method for a more complete assessment of  
 228 location errors. The SVD option for double difference locations can only solve for a significantly  
 229 lower number of earthquakes than the LSQR option. Nevertheless, we were able to apply the SVD  
 230 technique for all the sequences apart from the Rocca San Felice sequence. For this latter sequence,  
 231 discussed in detail in the Section 4, we estimated location uncertainties using a bootstrap strategy.  
 232 We realized 200 independent double difference location runs on subsets of events within the  
 233 sequence. Each subset was obtained by randomly extracting 150 events, 60 % of which belong to  
 234 the machine learning catalog. This constraint in the selection of the events in each subset ensures  
 235 a more robust linkage to the cluster, since the number of picks associated with templates is  
 236 generally larger than for template-matched events. We evaluated the location uncertainties from a  
 237 statistical analysis based on the distance of each event from the cluster centroid for all the runs  
 238 where that event was located. This procedure allows quantification of the dependency of the results  
 239 on the single subset. For the  $i$  – th event we estimated the uncertainty along the  $j$  – th direction  
 240 as  $err_j^i = median_{(p,m)} |(x_{j,p}^i - x_{j,p}^c) - (x_{j,m}^i - x_{j,m}^c)|$ , where  $p$  and  $m$  indicate two  
 241 independent runs in which the  $i$  – th event was located, and the superscript  $c$  refers to the cluster  
 242 centroid of the considered run. The robustness of these estimates has been verified observing  
 243 agreement with uncertainties from a SVD inversion for the subset of template events.

### 244 **3.2 Source Parameters**

245 We used a probabilistic inversion approach (Supino et al., 2019) for retrieving earthquake source  
 246 parameters (seismic moment  $M_0$  and corner frequency  $f_c$ ) from the S-wave displacement  
 247 amplitude spectra of relocated events. This technique is grounded in a Bayesian inversion of the

248 spectra and allows an exploration of the correlations among parameters with a robust estimation  
 249 of the uncertainties. The source is described by a generalized Brune model (Brune, 1970)

$$\tilde{S}(M_0, f_c, \gamma; f) = \frac{M_0}{1 + \left(\frac{f}{f_c}\right)^\gamma} \quad (1)$$

250 where the spectral fall-off at high-frequencies  $\gamma$  is considered as free parameter. The propagation  
 251 contribution is described by the term (e.g., Supino et al. 2019)

$$\tilde{G}(Q, f) = KAe^{-\pi fT/Q} \quad (2)$$

252 where  $T$  is the source-receiver travel-time,  $Q$  is the quality factor related to anelastic attenuation,  
 253  $A$  is the geometrical spreading (assumed as  $1/r$ , where  $r$  is the source-receiver distance) and

$$K = \frac{R_S F}{4\pi\rho\beta^3} \quad (3)$$

254 We assumed the average radiation pattern for S-waves  $R_S = 0.63$  (Boore & Boatwright 1984), a  
 255 free surface reflection coefficient of  $F = 2$ , the density  $\rho = 2700 \text{ kg/m}^3$  and the S-wave velocity  
 256  $\beta = 3027 \text{ m/s}$  (Zollo et al. 2014). After removing the instrumental response, the displacement  
 257 amplitude spectrum can be written as:

$$\tilde{U}(M_0, f_c, \gamma, Q; f) = \tilde{S}(M_0, f_c, \gamma; f) \cdot \tilde{G}(Q; f) \quad (4)$$

258 The modelling of the spectra requires a joint inversion for source parameters and quality factor,  
 259 which are strongly correlated. To reduce this correlation, we tried to evaluate the quality factor  
 260 separately from the inversion of source parameters. We started by considering the small events in  
 261 each sequence as empirical Green's functions (EGF). For those events the effective (source) corner  
 262 frequency is much larger than the apparent corner frequency of the anelastic attenuation low-pass  
 263 filter, and sometimes even larger than the Nyquist frequency of the records (in this case  $f_{Nyq} =$   
 264  $62.5 \text{ Hz}$ ). Considering the EGF spectra in the domain where  $f \ll f_c$ , the displacement spectrum  
 265 can be approximated as:

$$\tilde{U}_{EGF} = KAM_0 e^{-\pi fT/Q_{EGF}} \quad (5)$$

266 We selected events featuring local magnitude  $M_l < 1$  as EGFs and fit with a linear model  $\log \tilde{U}_{EGF}$   
 267 as a function of the frequency to retrieve  $M_0$  and  $Q_{EGF}$ . The frequency band selected for the fit

268 respects the constraint of a signal-to-noise ratio larger than 3.5 for each frequency in the band. The  
 269 value of  $Q_{EGF}$  is station dependent.

270 Since events in the same sequence share almost the same source-receiver path, we expect a  
 271 consistency in the  $Q_{EGF}$  estimates across the EGFs for the same station. For stations presenting at  
 272 least 5 estimates of  $Q_{EGF}$ , we evaluated the compatibility of the inferred values and used the mean  
 273 value to correct for anelastic attenuation.

274 For other stations, for which we have insufficient high-quality EGFs, we attempted to estimate a  
 275 sequence-dependent quality factor  $Q_{LOC}$  by exploring different values of the anelastic attenuation  
 276 around the average regional estimate  $Q_{REG} = 230$  (Zollo et al., 2014). Considering events with  
 277  $Ml > 1$ , we inverted the displacement amplitude spectra, and fixed the attenuation to one of the  
 278 following values  $Q = 100, 170, 230, 300, 400$  in different inversion runs. We compared the  
 279 average residuals resulting from the best solution for the source parameters in each run. We  
 280 selected as  $Q_{LOC}$  the  $Q$  value producing the lowest misfit, imposing a minimum number of 5  
 281 solutions per station. We finally kept  $Q = Q_{REG}$  for stations where neither  $Q_{EGF}$  nor  $Q_{LOC}$  could be  
 282 evaluated.

283 Finally, the inversion technique provided the seismic moment  $M_0$  (and the moment magnitude  $M_w$ )  
 284 for all the events, but corner frequencies only for events with  $Ml > 1$ . Quality of the solutions was  
 285 checked by analysing the shape of the a-posteriori probability density function related to the  
 286 estimated parameters. Solutions not showing peaked probability functions were discarded  
 287 following the strategy defined in Supino et al. (2019).

### 288 **3.3 Stress change model**

289 For events in the sequence for which we estimated both moment magnitude and corner frequency,  
 290 we computed the source radius  $a$  as (Madariaga, 1976):

$$a = k \frac{\beta}{f_c} \quad (6)$$

291 where  $k$  is a geometrical shape factor, which was assumed here as  $k = 0.37$  (Brune, 1970). We  
 292 derived the stress drop  $\Delta\sigma$  from seismic moment and the source radius (Keilis-Borok 1959) as:

$$\Delta\sigma = \frac{7}{16} \frac{M_0}{a^3} \quad (7)$$

293 We then evaluated the average stress drop  $\Delta\bar{\sigma}$  for the sequence as the mean value of the retrieved  
294 stress drops. We associated the average stress drop  $\Delta\bar{\sigma}$  with all other events in the sequence for  
295 which we were not able to estimate the corner frequency, and we used the above relationship to  
296 retrieve the event source radius.

297 We evaluated the rupture plane associated with the seismic sequence as the best-fit plane across  
298 the hypocenters of the events in the sequence. If the locations did not constrain a plane, we used  
299 the focal mechanism solutions from Palo et al. (2023) and selected the plane that is more consistent  
300 with the expected orientation of faults in the area. We finally mapped the stress change on the fault  
301 plane associated with the sequence, using the rupture model proposed by Andrews (1980) and a  
302 non-isotropic representation of the stiffness. Since in the rupture model neither the slip nor the  
303 stress drop is considered constant, we imposed the condition that the average stress drop within  
304 the crack from the Andrews model coincided with the event stress drop computed from the source  
305 parameters.

#### 306 **4 Results**

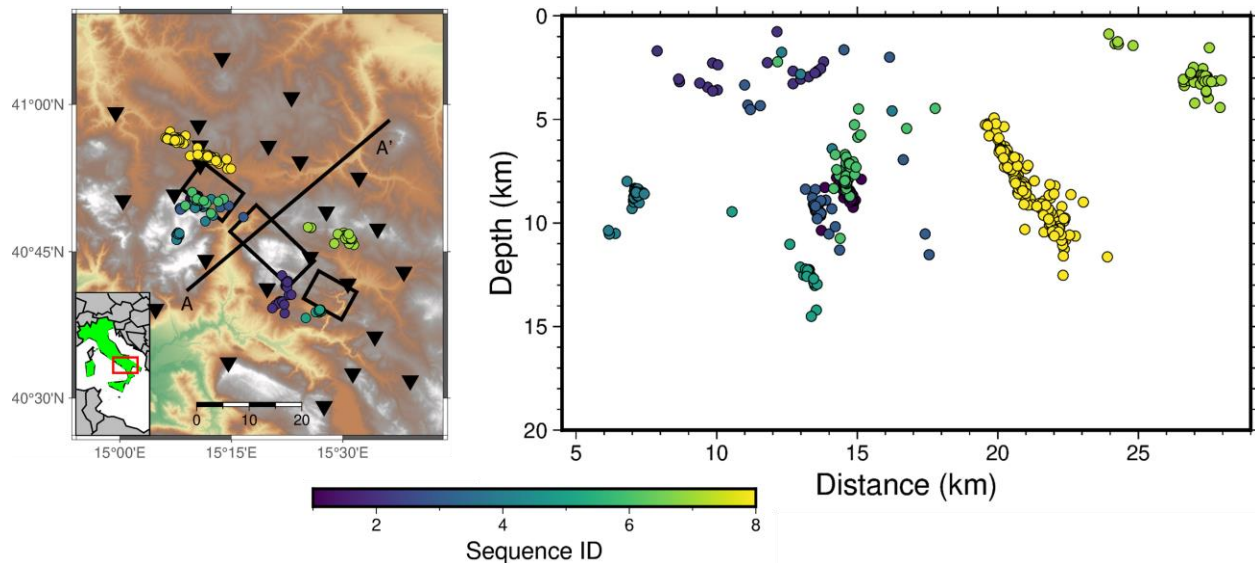
307 For all the enhanced catalogs related to the sequences in Scotto di Uccio et al. (2023), we computed  
308 absolute and (double difference) relative locations using NonLinLoc and HYPODD codes. Using  
309 the automatic phase arrival times provided by the integration of machine learning and template  
310 matching pickers, we obtained absolute locations for 1130 events ( $\sim 60\%$  of the detection catalog).  
311 The uncertainties can be as large as few kilometers, resulting into several tenths of second root-  
312 mean square (RMS) of travel time residuals. This uncertainty is enough to obscure the fault  
313 segments or patches on which the seismicity takes place. The number of absolute locations from  
314 the enhanced catalogs is 5 times larger than in the manual INFO bulletin and provides a wide set  
315 of catalog and cross-correlation delay times for earthquake relocation. When analyzing the single  
316 sequences, the improvement in the number of located earthquakes ranges from a factor 2.5 to 8.5.

317 Starting from the absolute positions of earthquakes in the enhanced catalogs, we achieved double  
318 difference relocation of 550 events total, from 8 out of the 10 seismic sequences analyzed in Scotto  
319 di Uccio et al. (2023). The two sequences for which we did not get relocations (IDX 7 and IDX 9

320 in Scotto di Uccio et al. 2023) feature the lowest number of detections (about 40 events). The total  
 321 number of relocated events represents  $\sim 30\%$  of the enhanced catalog. A similar fraction is  
 322 observed for each of the relocated sequences and results coherent with earthquake relocation of  
 323 other template matching derived catalogs (Cabrera et al. 2022, Ross et al. 2019), due to low signal-  
 324 to-noise ratio of small events leading to limited pick availability and triggered stations.

325 Figure 2 shows the double difference relocation of the earthquakes in the enhanced catalogs. In  
 326 the left panel we show the position of epicenters with respect to the seismic network. In the right  
 327 panel the hypocenters are projected along the vertical plane A-A' oriented perpendicular to the  
 328 trend of the Apennines (N40°E). This plane represents the direction orthogonal to the main  
 329 structures of the area, that generated the 1980 Irpinia earthquake. In Table S1 we report the label  
 330 of the sequences in this work with respect to the references in Scotto di Uccio et al. (2023).

331



332

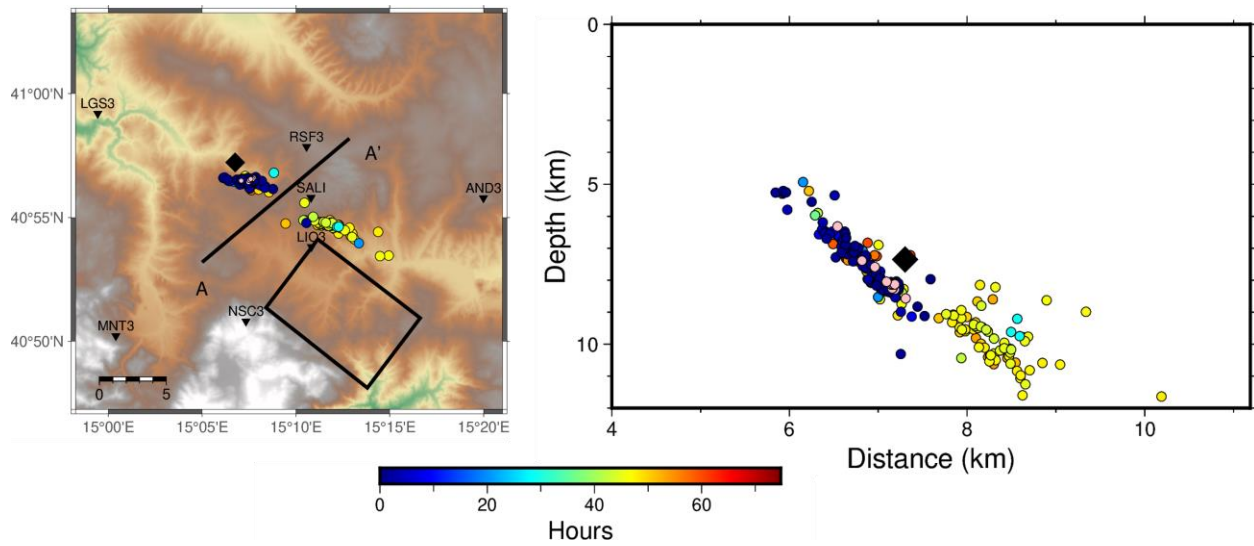
333 *Figure 2) Left panel: Epicentral location for the relocated events, colored according to the sequence IDX and*  
 334 *representation of the fault traces in the Irpinia area. Stations are shown with black triangles. Right panel: Cross-*  
 335 *section along the A-A' vertical plane, orthogonal to the main structure of the 1980 M6.9 earthquake for which rupture*  
 336 *planes are shown with black rectangles.*

337 The cross-section shows that the seismicity patterns feature clear alignments and a high degree of  
 338 clustering, highlighting km-sized structures that share similar dips. For all sequences, the spatial  
 339 extent of the sequences depicted by relocations is much greater than what expected from the total  
 340 released seismic moment.

341 The Rocca San Felice sequence, marked in Figure 2 with yellow dots (IDX 8) features the highest  
342 number of both detections and double difference located events ( $\sim 800$  and 250 events  
343 respectively). For this sequence, we were able to estimate absolute locations for about 60 % of the  
344 detections, with average horizontal and depth uncertainties of 1.5 km (average RMS residuals of  
345 0.4 s). We evaluated double difference relocations, limiting the analysis to events with at least 2  
346 P-picks and one S-pick among the three stations closest to the centroid of the sequence ( $\sim 300$   
347 located earthquakes). From about 97.5 k catalog differential times (47k for P phase, 50.5k for S  
348 phase) and 85k CC delay times (31k for P phase, 54k for S phase) we obtained a catalog of 250  
349 relocated events with median location uncertainties of 91 m, 31 m and 105 m in the East, North  
350 and vertical directions, respectively. When zooming on the sequence location (Figure 3 - left  
351 panel), the position of the epicenters clearly suggests the presence of two clusters, at 5 km of  
352 distance from each other. The projection of the seismicity along the vertical plane oriented  $N40^\circ E$   
353 (Figure 3 – right panel), indicates that the two clusters feature similar orientations but occurred at  
354 different depths: the shallower one is mostly confined between 6 km and 9 km, the deeper one  
355 between 9.5 km and 11 km. The two clusters were activated at different times during the sequence,  
356 as shown in Figure 3, where the colors denote the occurrence time of the events relative to the  
357 mainshock. The events occurred within the first two days of the mainshock illuminate a first 4-km  
358 long segment with a dip of  $55^\circ$ , coherently with the focal mechanism estimated by Festa et al.  
359 (2021). Two days after the main event, the occurrence of a  $M_l$  2.8 event activated a deeper  
360 secondary patch of slightly shorter extent with a similar orientation.

361 The presence of two separated clusters was not recognized in the previous work of Festa et al.  
362 (2021) and is supported by the change in the first station recording the P wave arrival, that occurred  
363 at the station RSF3 for events in the first cluster and at LIO3 for events in the second one. In Figure  
364 S2 we reported the vertical records, at the closest stations, for two events belonging to the two  
365 clusters. It is worth to note that the improvement in double difference location as compared to the  
366 results of Festa et al. (2021) comes from the combination of a deeper event catalog, but also from  
367 a larger number of picks per event. Indeed, for most of the events we were able to retrieve picks  
368 and waveforms also for the accelerometric station SALI, located close to the centroid epicenter,  
369 indicating that strong motion sensors can provide useful information even for microseismic events  
370 if their sensitivity is high enough (for SALI it is  $4.0 \text{ V/m/s}^2$ ).

371



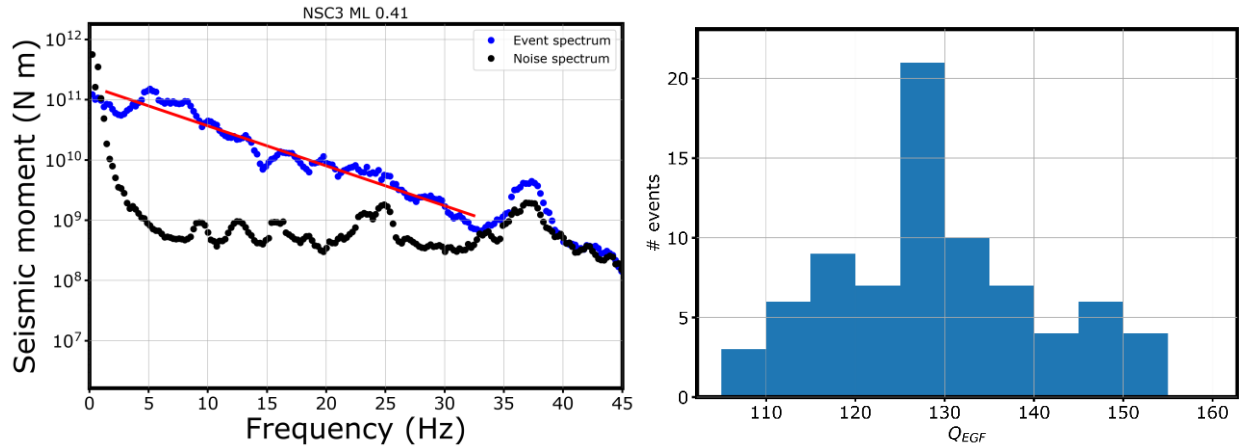
372

373 *Figure 3) Left panel: Spatio-temporal evolution of the epicenters for the Rocca San Felice seismic sequence (IDX 8),*  
 374 *colored according to the occurrence time from the main event. Foreshocks are represented with pink circles and the*  
 375 *main event is represented with a black diamond. Right panel: Cross-section along the vertical plane as in Figure 2,*  
 376 *colored according to the occurrence time from the main event.*

377 We inverted the displacement spectra of the relocated events to infer the seismic moment  $M_0$  (and  
 378 hence the moment magnitude  $M_w$ ), the corner frequency  $f_c$  and the quality factor  $Q$  as output. For  
 379 each sequence, we separated events with local magnitude above and below 1.0, according to the  
 380 estimates of Scotto di Uccio et al. (2023) as described in Section 2. We then estimated  $M_0$  and  $Q$   
 381 for the events in the sequence below the magnitude threshold, considered as EGFs, and used these  
 382 parameters to infer the moment and the corner frequency of the larger events (above the threshold).

383 Here, we illustrate all the steps in our analysis for the Rocca San Felice sequence, which we also  
 384 applied to all the other sequences. For the stations closest to the sequence, recording many small  
 385 magnitude events ( $M_l < 1$ ), we tried to estimate the quality factor  $Q_{EGF}$  by fitting the logarithm  
 386 of the displacement spectra as a linear function of the frequency. For each EGF, we perform the fit  
 387 in the frequency band where the signal-to-noise ratio exceeds the threshold of 3.5. As an example,  
 388 we show in Figure 4 - left panel- the displacement amplitude spectrum and the corresponding noise  
 389 spectrum for a  $M_l 0.41 \pm 0.10$  earthquake at the station NSC3 ( $\sim 11$  km distance from the main  
 390 event). We estimated the quality factor for the considered earthquake from the slope of the linear  
 391 fit (Figure 4, left panel), whose intercept is proportional to the seismic moment. We thus estimated

392 the quality factor  $Q_{EGF}$  from the fit of each candidate EGF. An example of  $Q_{EGF}$  distribution (for  
 393 the station NSC3) is reported in the right panel of Figure 4. We observe a peaked Gaussian-like  
 394 distribution, which is typical of stations providing a large number of estimates for the quality  
 395 factor. We extracted the weighted mean of individual  $Q_{EGF}$  values using the inverse of the fit  
 396 residuals as weighting factors, to describe the quality factor  $\bar{Q}_{EGF}$  for that station-sequence couple.



397

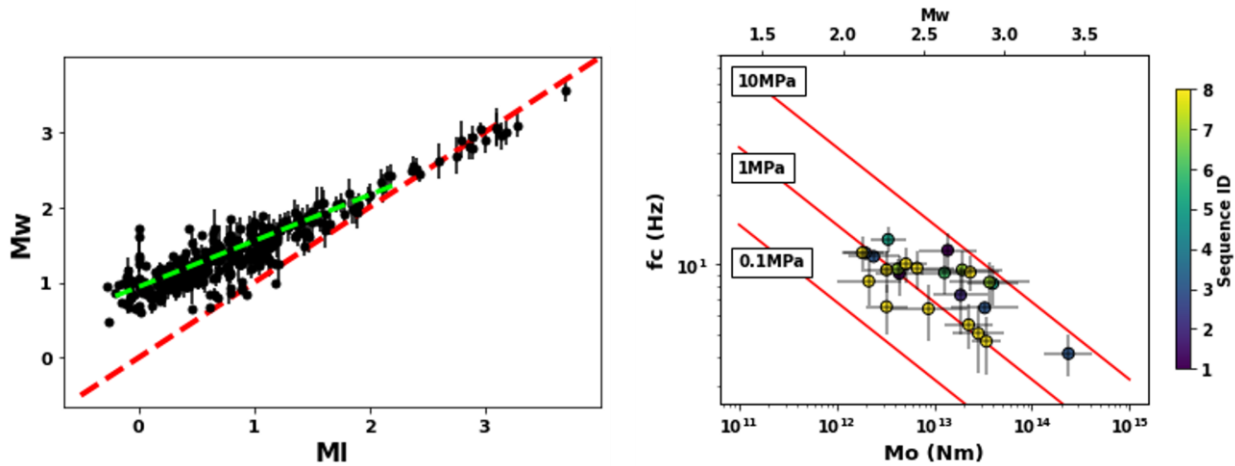
398 *Figure 4) Left panel:  $Q_{EGF}$  estimation from linear fit (red solid line) of the logarithm of the displacement event spectrum*  
 399 *(blue dots) as a function of the linear frequency, for a  $M_l = 0.41$  earthquake. Noise spectrum is reported as black*  
 400 *dots. Right panel: histogram of the  $Q_{EGF}$  for the events  $M_l < 1$  in the Rocca San Felice sequence (IDX 8) at NSC3*  
 401 *station*

402 For the example of Figure 4, we estimated  $\bar{Q}_{EGF} = 130 \pm 12$  for NSC3, which is smaller than  
 403 the regional estimation provided by Zollo et al. (2014).

404 For the stations lacking sufficient high-quality EGFs, we attempted to extract a local quality factor  
 405  $Q_{LOC}$  by performing several inversions with different, fixed  $Q_s$  values. We then assumed as the  
 406 most suitable value of  $Q$  the one that resulted in the lowest average RMS residuals. In the case of  
 407 the Rocca San Felice sequence, this procedure allowed estimation of the quality factor for five  
 408 stations (COL3, SCL3, SFL3, SNR3, SSB3). For stations where neither  $Q_{EGF}$  nor  $Q_{LOC}$  was  
 409 estimated, we considered the regional value of the area for the quality factor ( $Q_s = 230$ , Zollo et  
 410 al. 2014). After the estimation of the quality factor from the EGF, we attempted to estimate the  
 411 source parameters for events with  $M_l > 1$ , by fitting the spectra with the generalized Brune model.  
 412 In Figure S3 we report the fit results for a  $M_l = 2.8$  event at three stations. In Figure S3 – left panel  
 413 – we represent the fit of the displacement spectrum at the station NSC3, where we used an EGF

414 derived quality factor ( $Q_{EGF} = 130$ ). In the central panel we report the results for the station SCL3  
 415 ( $\sim 43$  km from the main event) where we estimated a quality factor  $Q_{LOC} = 300$ , higher than the  
 416 average estimate for the area. We note that in this latter case, the average value ( $Q = 230$ ) provides  
 417 unreliably large corner frequencies (as compared to the values obtained at other stations), close to  
 418 the upper limit of the frequency band used for the inversion. In the right panel, we show the fit for  
 419 the station VDS3 ( $\sim 38$  km from the main event), for which we used the regional value  $Q_{REG} =$   
 420 230.

421 For the Rocca San Felice seismic sequence, we retrieved the seismic moment  $M_0$  for 45 % of the  
 422 located events, while we globally estimated the seismic moment for 236 out of the 550 relocated  
 423 events ( $\sim 60\%$ ). In Figure 5 - left panel we report the distribution of the moment magnitude  $M_w$   
 424 (Hanks and Kanamori, 1979), against the local magnitude  $M_l$ , as evaluated in Scotto di Uccio et  
 425 al. (2023), considering all the events for which an estimation of the seismic moment was available.  
 426 The red line marks the 1:1 trend between  $M_l$  and  $M_w$ .



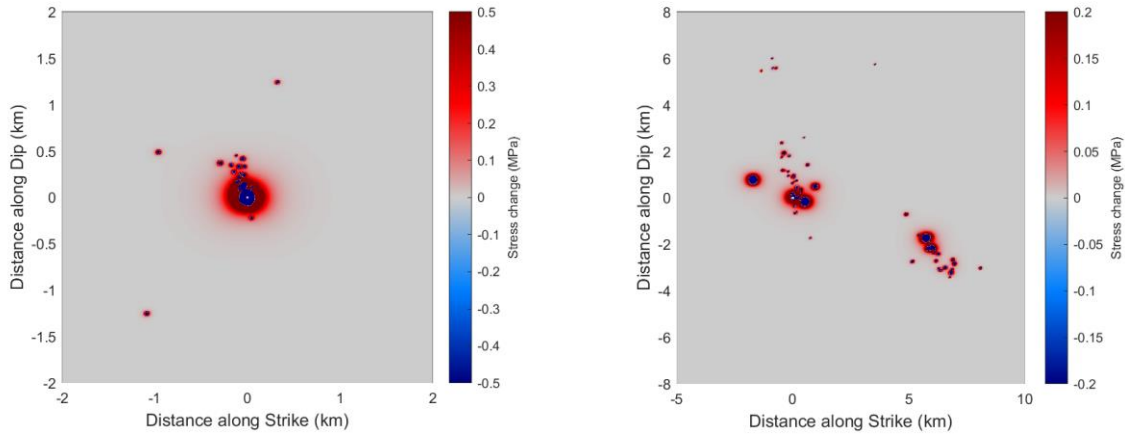
427  
 428 *Figure 5) Left panel:  $M_w - M_l$  distribution, with the 1:1 relation scaling reported as dashed red line. For  $M_l < 2$*   
 429 *earthquakes, we observed  $M_w = 0.89 (\pm 0.03) + 0.62 (\pm 0.02)M_l$  (green dashed line). Right panel: Distribution of*  
 430 *source parameters for  $M_w > 2$ , colored according to sequence IDX, with theoretical constant stress drops scaling of*  
 431 *0.1 MPa, 1 MPa and 10 MPa (red solid lines)*

432 We recognize two trends between the magnitude scales: for  $M_l < 2$  the distribution strongly  
 433 deviates from the 1:1 scaling relation. Evaluating the average value of  $M_w$  in different  $M_l$  bins of  
 434 width 0.2 and performing a linear fit between the two quantities, we retrieved  $M_w = a + b * M_l =$   
 435  $0.89 (\pm 0.03) + 0.62 (\pm 0.02)M_l$  (the linear fit curve is reported with a green dashed line). The

436 estimated slope agrees with the predictions of Deichmann (2017), which indicated a saturation of  
437 the event duration in the local magnitude computation due to the anelastic attenuation, resulting  
438 into the scaling  $M_w = C + \frac{2}{3} M_l$ . For  $M_l > 2$ , the distribution follows the 1:1 scaling trend  
439 between  $M_l$  and  $M_w$ , as also found by Zollo et al. (2014). In the right panel of Figure 5 we reported  
440 the  $\log M_0 - \log f_c$  distribution, with red straight lines marking the theoretical trends obtained  
441 assuming characteristic stress drop values of  $\Delta\sigma = 100kPa, 1MPa$  and  $10 MPa$ . The single  
442 station corner frequencies have been averaged considering the relative uncertainty of the estimate.  
443 As a result, we determined seismic moment and corner frequency for events with moment  
444 magnitude  $M_w > 2.0$ , while for events below this magnitude, the solution for the corner frequency  
445 was not constrained (Supino et al. 2019). For the resolved events, the distribution of the corner  
446 frequencies with moment appears to follow a nearly linear trend, with stress drop ranging between  
447 1-3 MPa. For the Rocca San Felice sequence, yellow marks in the right panel of Figure 5, the  
448 average  $\Delta\sigma$  resulted to be  $\sim 1.0 MPa$

449 We evaluated the source size for all the events for which we estimated the seismic moment, either  
450 by considering the retrieved corner frequency or by assuming self-similarity. The former condition  
451 applies to the largest magnitude events in the sequences, the latter for lower magnitude events. For  
452 each sequence, we assessed the best fitting plane from earthquake locations, and represented the  
453 static stress released by single events onto this plane (Andrews et al. 1980) along the strike and  
454 dip directions. For almost all the sequences (IDXs 1 to 7) the stress model suggests static stress  
455 release as a trigger mechanism, with small events mainly concentrated in or around the area  
456 affected by stress changes due to the main events in the sequence. As an example, we report in  
457 Figure 6 – left panel - the stress release model for a seismic sequence featuring a  $M_l$  2.9 main event  
458 (IDX 1 in Figure 2). We observe a single km-sized patch mainly oriented along the dip direction,  
459 with earthquakes occurring within the volume interested by the main event. We retrieved similar  
460 dip – oriented trends also for the other considered sequences. An interesting case is represented by  
461 the Rocca San Felice seismic sequence (IDX 8 in Figure 2 and in Figure 3), illustrated in the right  
462 panel of Figure 6. For this sequence, we observe two seismicity patterns activated at different times  
463 (the main event  $M_l$  3.0 involved the leftmost patch, and the seismicity migrated along the rightmost  
464 segment almost two days after the mainshock with the occurrence of a  $M_l$  2.8 earthquake). In both

465 clusters we still observe a predominant orientation along the dip direction. In the following  
 466 discussion, we investigate the mechanical connection between these two patches.



467  
 468 *Figure 6) Stress released model for the IDX 1 (left panel) and IDX 8 (Rocca San Felice, right panel) sequence. In both*  
 469 *representations, we observe earthquakes occurring within the volume interested by the main event, with preferentially*  
 470 *dip-oriented patches.*

## 471 **5 Discussion**

472 Catalog enhancement using advanced detection techniques allows an increase in the number of  
 473 earthquakes up to an order of magnitude as compared to ordinary seismic catalogs. For seismic  
 474 sequences in the normal fault system of Southern Apennines (Italy), we find an enhancement of a  
 475 factor  $\sim 7$  with respect to the number of earthquakes manually detected by network operators  
 476 (Scotto di Uccio et al. 2023). The improvement in the magnitude of completeness of these deep  
 477 catalogs makes it possible to monitor variations in the statistical parameters describing the  
 478 seismicity, such as the b-value of the Gutenberg-Richter relation (Beroza et al. 2021). These  
 479 changes can only be roughly indicative of variations in the mechanical properties underlying the  
 480 faults, such as the differential stress (Scholz 2015); however, the evaluation and the consequent  
 481 use of these parameters for interpreting the evolution of the sequences is still debated, in part due  
 482 to biases in the magnitude estimates (Gulia & Wiemer 2019, Hermann & Marzocchi 2021, Mancini  
 483 et al. 2022).

484 The clearer view of the manifestation of the mechanical properties of structures in the form of  
 485 earthquake sequences can be achieved through accurate location and source parameter estimation;  
 486 however, the generally low signal-to-noise ratio of the new events in the enhanced catalogs, does

487 not fully translate into an equal increase in the number of earthquakes that can be accurately  
488 located. For seismic sequences in Irpinia, we retrieved double difference locations for  $\sim 30\%$   
489 events, a fraction similar or slightly larger than the percentage resulting from template matching  
490 derived catalogs (Ross et al. 2019, Simon et al. 2021, Cabrera et al. 2022). This reduction in the  
491 number of well-located events is driven by the different impact of the waveform similarity during  
492 the detection and the location phases. Template matching detection algorithms leverage on stacked  
493 cross-correlations across the entire network (Chamberlain et al. 2018, Vuan et al. 2018), resulting  
494 in a global similarity value, to which stations with both high and low cross-correlation values  
495 contribute. High-quality thresholds on the similarity coefficient for cross-correlation differential  
496 travel times requested by accurate double difference locations (Michele et al. 2020, Waldhauser et  
497 al. 2021), limit the number of available stations, especially for low magnitude events. Although  
498 the catalog of events located with double differences is only twice larger than the manual catalog,  
499 the improvement in cluster definition and spatial resolution is much more significant, allowing the  
500 identification of alignments and structures at kilometric scale, that were not clearly illuminated  
501 from the manual catalog (Palo et al. 2023), owing to the wide increase in the number of differential  
502 travel-times. As an example, for the Rocca San Felice sequence, we reported more than one order  
503 of magnitude more differential travel-times compared to the ones extracted from the manual  
504 catalog (Festa et al. 2021).

505 When moving to the moment magnitude estimation, the number of events in the enhanced catalog  
506 that can be characterized further decreases, to 15% of the detections (or 60% of the relocated  
507 events). Furthermore, we resolved the corner frequencies only for events with moment magnitude  
508  $M_w > 2.0$  already present in the network catalog due to the limited available frequency bandwidth  
509 for the inversion related to the signal-to-noise ratio and data sampling rate. Nevertheless, we were  
510 able to reduce the epistemic uncertainty in the estimate of source parameters due to the  
511 propagation, using small earthquakes as empirical Green's functions.

512 Averaging over all sequences, we found an average stress drop of  $\Delta\sigma = 2.35 \text{ MPa}$ ; its variability  
513 across sequences, estimated by the standard deviation is  $s_{\Delta\sigma} = 0.87 \text{ MPa}$ . The stress drop found  
514 here is one order of magnitude larger than the stress drop retrieved for the background seismicity  
515 in the area by Zollo et al. (2014), who used a similar inversion strategy and an independent catalog  
516 not influenced by the sequences studied here. Since they derived the average stress drop using the

517 Madariaga model (Madariaga 1976), when converting that value into an equivalent Brune's stress  
518 drop, they obtained a median value of  $\Delta\sigma = 0.26 \text{ MPa}$ . This difference indicates that the release  
519 of stress during sequences likely occurs in more compact asperities that can be associated with a  
520 higher coupling than for background seismicity (Chen & Shearer 2012).

521 The stress drops we retrieved for these seismic sequences are comparable to the estimate of  
522  $3.5 \text{ MPa}$ , achieved for the 1980, M 6.9 Irpinia earthquake (Deschamps & King 1983, Bernard &  
523 Zollo 1989). When mapping the seismic sequences at depth, their location is generally not  
524 compatible with faults that hosted the 1980 event - based on either the fault trace at the surface  
525 (Westaway & Jackson 1987) or the event dip and geometry estimated from seismic and levelling  
526 data (Bernard and Zollo 1989, Amoroso et al. 2005). This indicates that seismic sequences ruptured  
527 small patches of secondary segments, as compared to the main structure of the M 6.9 earthquake.

528 The investigated area undergoes a strain-rate of  $\sim 100 \text{ nstrain/yr}$  and an increase of  $3 \text{ mm/yr}$  over  
529  $30 \text{ km}$  along the axial sector of the Apennines. All the investigated sequences fall within the  
530 actively deforming area, providing important insight into the geometry of structures potentially  
531 activated during larger magnitude events. The Rocca San Felice sequence, roughly aligned along  
532 the northwestward continuation of the complex multi-segment fault system activated during the M  
533 6.9 earthquake, illuminates a NE-dipping structure whose geometry is favorably oriented for  
534 seismic release of NE-SW accumulated interseismic strain (Figure 1). This structure is not mapped  
535 in the catalog of the Italian seismogenic Faults (DISS, <https://diss.ingv.it/>), which should motivate  
536 additional investigation of the long-term, seismogenic behavior of the structures illuminated by  
537 local seismic sequences.

538 We found differences in the stress drops associated with sequences, with an increase of the stress  
539 drop moving from North to South in the Irpinia region, as also shown by Picozzi et al. (2022),  
540 whose catalog contains all the events with magnitude larger than 1.5 for the area. We found average  
541 stress drops of  $\Delta\sigma_N = 2.0 \text{ MPa}$  in the Northern sector (Cervialto Fault area, the initial rupturing  
542 segment of the 1980 earthquake) and  $\Delta\sigma_S = 2.8 \text{ MPa}$  in the Southern Sector (San Gregorio  
543 Magno Fault area, i.e., on the second rupturing segment of the 1980 earthquake). Tomographic  
544 images in velocity (Amoroso et al. 2014, Improta et al. 2014, Vassallo et al. 2016) and anelastic  
545 attenuation ( $Q_p$ ,  $Q_s$ ; Amoroso et al. 2017) coupled with rock physics modelling indicate the  
546 presence of pressurized fluids in the area of microseismicity. Differences in the stress drops

547 between the two areas could be associated with the different fluid content and fraction. In the  
548 Southern sector rock physics modelling indicates the presence of a mixture brine-CO<sub>2</sub> (Amoroso  
549 et al. 2017). The large, extended low V<sub>p</sub>/V<sub>s</sub> anomaly in tomographic images in the northern sector  
550 indicates a pressurized reservoir of fluids, associated with the large natural emission of low-  
551 temperature CO<sub>2</sub> at the Mefite d'Ansanto, Rocca San Felice site (Chiodini et al. 2010).

552 Several studies in the area indicate a correlation between shallow stress changes in the karst aquifer  
553 induced by hydrological loading via the poroelastic response of the rocks and deep seismicity  
554 (D'Agostino et al. 2018). Although most of the sequences occurred during the maximum aquifer  
555 charge, we cannot infer a clear link between stress changes in the shallow water table and the  
556 occurrence of the sequences. However, the small amount of stress perturbation that propagates at  
557 depth (D'Agostino et al., 2018) compared to the large stress drops retrieved during sequences may  
558 indicate an elastic coupling between the shallow Mesozoic carbonates and the underlying Apulian  
559 platform beneath the *mélange*, and a critical state of these small patches, that are prone to generate  
560 the sequences with a stress excess that is only a few percent of the stress drop required to nucleate  
561 events.

562 When mapping the stress change on the fault plane associated with the sequences, most of the  
563 events appear connected, indicating that the sequences ruptured single patches along the fault  
564 plane. The inter-event distance, compared to the size of the events, suggests that the dominant  
565 triggering mechanism within the sequences is static stress transfer, that allows the nucleation of  
566 individual events in the sequence. Nevertheless, an important feature retrieved here is that the  
567 distribution of the events is not isotropic around the main events of the sequences, but small events  
568 tend to align dominantly along the dip direction, which also corresponds to the slip direction, for  
569 normal faults. Specific patterns for sequences along the direction of the slip have been observed  
570 in strike-slip environments (Rubin et al. 1999, Shearer 2002). Lineation of the seismicity along the  
571 major faults in California have been interpreted as the boundary between locked and creeping  
572 domains (Rubin et al. 1999, Rubinstein and Beroza 2007). In the normal fault environment of  
573 Southern Apennines also, evolution of the seismicity during the sequences is controlled by slip and  
574 cannot be explained by the anisotropic stress release after the event (Andrews 1980, see also the  
575 stress changes of Figure 6). Fault roughness, modulated by repeated stick slip episodes may  
576 determine predominant patterns at the scale of the microseismicity observed here (10 – 100m),

577 with striations mainly oriented along the dip direction (Candela et al. 2011). Corrugated faults  
578 behave as geometrical asperities and can localize deformation hosting stick-slip episodes at small  
579 scales (few centimeters of slip) (Resor and Meer 2009). Fault roughness and geometrical barriers  
580 at this scale may also impede small events from growing into larger magnitude earthquakes (Sagy  
581 et al. 2007, Marshall and Morris 2012). These strips can also favor upward migration of fluids,  
582 although we cannot discern a signature of diffusion-dominated processes from the space-time  
583 evolution of the sequences.

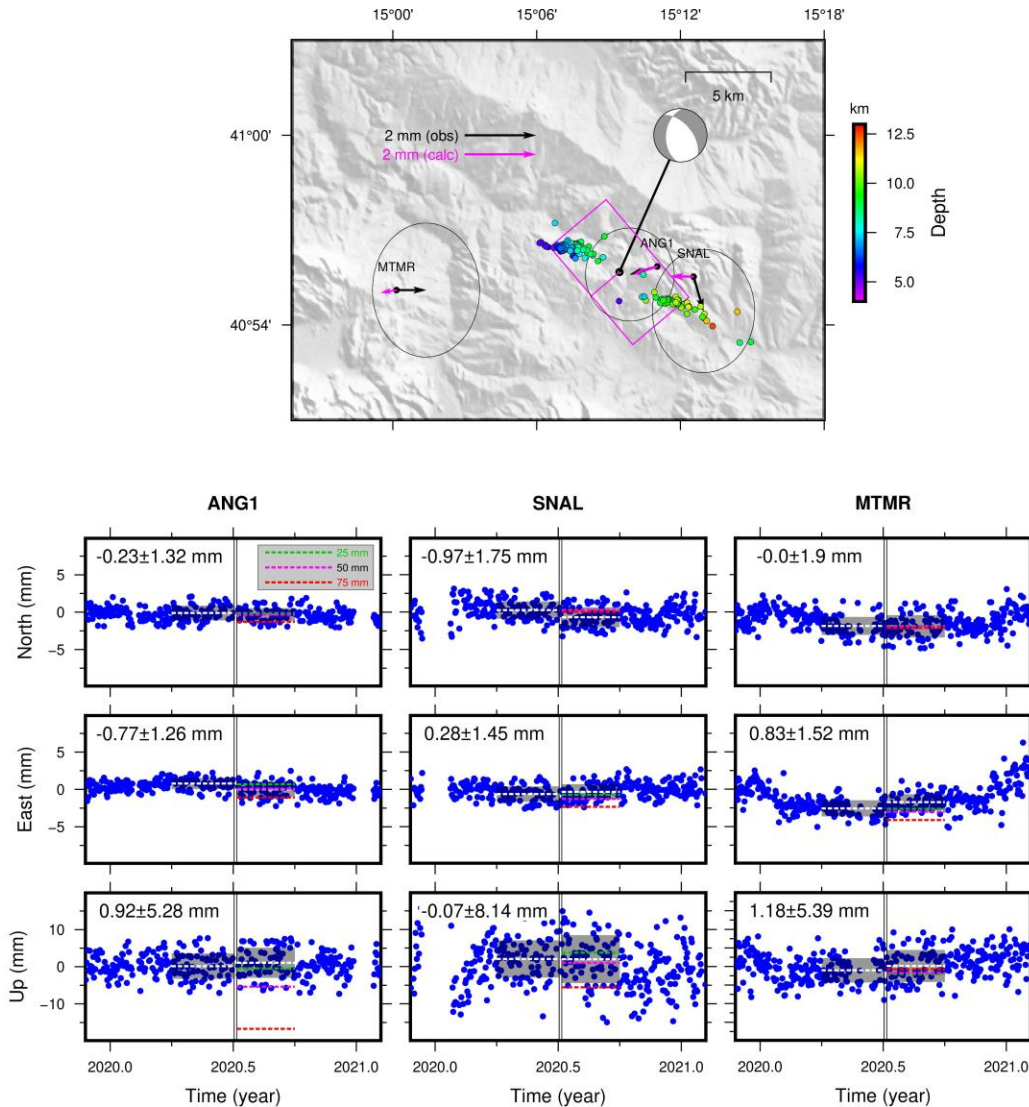
584 The occurrence of aseismic slip episodes nearby the lineations could also be the cause for the  
585 along-dip evolution of the seismicity and might explain the longer extent compared to the released  
586 seismic moment. Aseismic transients have been already observed in normal fault environments  
587 during the occurrence of larger seismic sequences (Gualandi et al. 2017, Kaviris et al. 2021).  
588 However, for the sequences analyzed here, geodetic data has not detected aseismic transients at  
589 this space-time scale during the sequences analyzed in this study.

590 The Rocca San Felice sequence shows the activation of two parallel clusters, oriented along the  
591 dip direction, but about 5 km apart. The two clusters featured main events of similar magnitude  
592 ( $M_l$  3.0 and  $M_l$  2.8, respectively), a kilometeric size extension along the dip (4 km and 2 km), with  
593 the first evolving preferentially up-dip, the second one downdip. The second cluster was activated  
594 about two days after the first sequence. As shown in Figure 6, the stress perturbation associated  
595 with the first sequence cannot be responsible for the activation of the second patch. Also, the lack  
596 of seismicity between the two segments does not support the hypothesis of fluid migration as  
597 responsible for triggering the second cluster. According to the rate of occurrence of independent  
598 events with  $M_l > 2.5$  in the northern part of the region ( $\lambda = 2.1 * 10^{-3} ev/day$ ), we estimated  
599 the probability of occurrence of two independent events within 2 days as about 0.4%.

600 We also tested the hypothesis of aseismic slip between the two seismicity clusters of this sequence.  
601 We assess the evolution of the displacement at the three closest GPS stations SNAL, MTMR,  
602 ANG1, the first two belonging to the INGV-RING network, the latter to the Regione Campania.  
603 The time series of daily coordinates (see D'Agostino et al., 2020 for details of GPS data  
604 processing) at the three stations have been checked for possible offsets across the seismic  
605 sequence. Evaluating the average positions in North, East and vertical coordinates, before and after

606 the Rocca San Felice sequence, we could not find significant static offsets within the estimated  
 607 error (Figure 7).

608



609 *Figure 7) Upper panel: map of the GPS stations near the Rocca San Felice seismic sequence and associated*  
 610 *displacements. The vectors show the horizontal displacements with one sigma error ellipses, from the static offset*  
 611 *during the seismic sequence. Circles represent events of the sequence color-coded with depth. Three different synthetic*  
 612 *scenarios were evaluated assuming increasing slip (25, 50, 75 mm), with geometry and kinematics from Festa et al.,*  
 613 *2021. The surface displacements produced by a slip of 50 mm on the fault drawn with purple lines is shown in the*  
 614 *map (purple arrows). Lower panel. GPS position time series and average positions (white dashed lines) before and*  
 615 *after the seismic sequence, with 1-sigma error shown with grey shading. Calculated displacements are also shown*  
 616 *(dashed lines) for the 25mm (green), 50mm (purple) and 75 mm (red) dislocation scenarios.*

617

618 We assessed the maximum average slip allowed on a deep dislocation whose displacement on the  
619 surface would not emerge from the noise level at the three GPS stations. We centered the potential  
620 aseismic dislocation between the two clusters and used the fault geometry and kinematics inferred  
621 by the composite focal mechanism solution of Festa et al. (2021) and calculated the surface  
622 displacements using the Okada techniques (Okada 1992). We tested a range of uniform slip on the  
623 dislocation between 25 and 75 mm, assuming constant strain drop of  $10^{-5}$ . The relatively deep  
624 position of the dislocation centroid between the two clusters ( $\sim 8$  km) allows slip on the deep  
625 dislocations up to 50 mm without detection at the surface (Figure 7). For slip larger than 50 mm  
626 the non-linear increase of cumulative seismic moment determines surface displacements outside  
627 the range of allowed offsets. Thus, an aseismic event of  $M_w \sim 5.0$  could have occurred during the  
628 sequence, transferring stress across the two asperities without producing a signal that would have  
629 been visible at the GPS stations.

## 630 **6 Conclusions**

631 In this work we presented a comprehensive analysis of seismic sequences through accurate  
632 earthquake location and source parameters estimation of enhanced catalogs (Scotto di Uccio et al.  
633 2023). Selecting machine learning and cross-correlation phase arrival times, we retrieved double  
634 difference locations for  $\sim 30\%$  of the events. The relocated seismicity revealed that seismic  
635 sequences involve kilometeric-scale structures, featuring a NW-SE dip and larger extent than  
636 expected from the magnitude of the mainshocks. While location of microseismicity usually relies  
637 on the use of records from velocimetric sensors, in this work the resolution of hypocenters  
638 benefited from phase arrival times determined on accelerometers located close to the main events  
639 of the sequences. Accelerometers can thus provide important arrival time information that is  
640 comparable in quality to velocimetric stations, improving the location results. For the relocated  
641 earthquakes, we estimated the source parameters (seismic moment  $M_0$ , corner frequency  $f_c$ )  
642 through a probabilistic inversion of the displacement spectra (Supino et al. 2019), and the resulting  
643 source size  $r$  and stress drop  $\Delta\sigma$ , assuming the generalized Brune model, finally mapping the stress  
644 change along the fault plane. We estimated the moment magnitude for 60% of the relocated events  
645 and we resolved the corner frequencies only for earthquakes with  $M_w > 2.0$ , using low-magnitude  
646 events as EGFs. We observed  $\Delta\sigma$  spanning the range  $[0.9 - 5.4]$  MPa, within the interval proposed  
647 for earthquakes in the Irpinia area (Picozzi et al. 2021) and source radius for the main events varies

648 from 105 – 235 m. We observed differences in the stress drops associated with sequences, with an  
649 increase of the stress drop from North to South in the Irpinia region, likely associated to the  
650 different fluid content and fraction. When mapping the stress change on the fault plane associated  
651 with the sequences, most of the events appear connected, indicating that the sequences ruptured  
652 single, contiguous patches along the fault plane. The inter-event distance, compared to the size of  
653 the events, suggests that the dominant triggering mechanism within the sequences is the (static)  
654 stress transfer, that allows the nucleation of individual events in the sequence. Alignment of events  
655 mainly along the dip direction indicates a slip dominated mechanism in the evolution of the  
656 seismicity, which could be associated with different fault roughness in the directions of the dip and  
657 strikes. Lineations in the definition of the seismicity might indicate aseismic transients occurring  
658 at the same time of the sequences. These transients could explain the migration of the seismicity  
659 from one cluster to the other one during the Rocca San Felice sequence. Although GPS data from  
660 stations located just above the sequence do not contain offsets indicative of such transients, a Mw  
661 5 aseismic event could have occurred at the sequence depth, without producing a signal emerging  
662 from the noise.

### 663 **Open Research**

664 Seismic products from the Irpinia Near Fault Observatory can be accessed through the Irpinia  
665 Seismic Network website (<https://isnet.unina.it>). Seismic data from INFO can be accessed through  
666 EIDA portal (<https://eida.ingv.it/it/>), network code IX or via the EPOS portal ([https://www.ics-](https://www.ics-c.epos-eu.org/)  
667 [c.epos-eu.org/](https://www.ics-c.epos-eu.org/)). GNSS data are accessible through the INGV website  
668 <ftp://bancadati2.gm.ingv.it:2121/OUTGOING/RINEX30/RING/>. Earthquake relocations were  
669 performed using NonLinLoc (<https://github.com/alomax/NonLinLoc>) and HYPODD  
670 (<https://www.ldeo.columbia.edu/~felixw/hypoDD.html>). Catalogs of the analyzed events are  
671 available at the following link: <https://zenodo.org/records/10441456> (Scotto di Uccio & Festa,  
672 2023) Maps in Figure 2 and Figure 3 were made using PyGMT (Uieda et al., 2021). Figure 4 and  
673 Figure 5 were produced using Matplotlib (Hunter, J.D., 2007). Figure 6 was produced using  
674 Matlab.

675

676

677 **References**

- 678 Abercrombie, R. E., & Rice, J. R. (2005). Can observations of earthquake scaling constrain slip  
679 weakening?. *Geophysical Journal International*, *162*(2), 406-424.
- 680 Abercrombie, R. E. (2015). Investigating uncertainties in empirical Green's function analysis of  
681 earthquake source parameters. *Journal of Geophysical Research: Solid Earth*, *120*(6), 4263-4277.
- 682 Abercrombie, R. E. (1995). Earthquake source scaling relationships from -1 to 5 ML using  
683 seismograms recorded at 2.5-km depth. *Journal of Geophysical Research: Solid Earth*, *100*(B12),  
684 24015-24036.
- 685 Amoroso, O., Ascione, A., Mazzoli, S., Virieux, J., & Zollo, A. (2014). Seismic imaging of a fluid  
686 storage in the actively extending Apennine mountain belt, southern Italy. *Geophysical Research  
687 Letters*, *41*(11), 3802-3809.
- 688 Amoroso, O., Russo, G., De Landro, G., Zollo, A., Garambois, S., Mazzoli, S., ... & Virieux, J.  
689 (2017). From velocity and attenuation tomography to rock physical modeling: Inferences on fluid-  
690 driven earthquake processes at the Irpinia fault system in southern Italy. *Geophysical Research  
691 Letters*, *44*(13), 6752-6760.
- 692 Amoruso, A., Crescentini, L., D'Anastasio, E., & De Martini, P. M. (2005). Clues of postseismic  
693 relaxation for the 1915 Fucino earthquake (central Italy) from modeling of leveling  
694 data. *Geophysical Research Letters*, *32*(22).
- 695 Andrews, D. J. (1980). A stochastic fault model: 1. Static case. *Journal of Geophysical Research:  
696 Solid Earth*, *85*(B7), 3867-3877.
- 697 Bernard, P., & Zollo, A. (1989). The Irpinia (Italy) 1980 earthquake: detailed analysis of a complex  
698 normal faulting. *Journal of Geophysical Research: Solid Earth*, *94*(B2), 1631-1647.
- 699 Beroza, G. C., Segou, M., & Mostafa Mousavi, S. (2021). Machine learning and earthquake  
700 forecasting—next steps. *Nature communications*, *12*(1), 4761.
- 701 Boore, D. M., & Boatwright, J. (1984). Average body-wave radiation coefficients. *Bulletin of the  
702 Seismological Society of America*, *74*(5), 1615-1621.
- 703 Brune, J. N. (1970). Tectonic stress and the spectra of seismic shear waves from  
704 earthquakes. *Journal of geophysical research*, *75*(26), 4997-5009.

- 705 Cabrera, L., Poli, P., & Frank, W. B. (2022). Tracking the spatio-temporal evolution of foreshocks  
706 preceding the Mw 6.1 2009 L'Aquila earthquake. *Journal of Geophysical Research: Solid*  
707 *Earth*, 127(3), e2021JB023888.
- 708 Candela, T., Renard, F., Schmittbuhl, J., Bouchon, M., & Brodsky, E. E. (2011). Fault slip  
709 distribution and fault roughness. *Geophysical Journal International*, 187(2), 959-968.
- 710 Chamberlain, C. J., Hopp, C. J., Boese, C. M., Warren-Smith, E., Chambers, D., Chu, S. X., ... &  
711 Townend, J. (2018). EQcorrscan: Repeating and near-repeating earthquake detection and analysis  
712 in Python. *Seismological Research Letters*, 89(1), 173-181.
- 713 Chen, X., Shearer, P. M., & Abercrombie, R. E. (2012). Spatial migration of earthquakes within  
714 seismic clusters in Southern California: Evidence for fluid diffusion. *Journal of Geophysical*  
715 *Research: Solid Earth*, 117(B4).
- 716 Chiaraluce, L., Valoroso, L., Anselmi, M., Bagh, S., & Chiarabba, C. (2009). A decade of passive  
717 seismic monitoring experiments with local networks in four Italian  
718 regions. *Tectonophysics*, 476(1-2), 85-98.
- 719 Chiaraluce, L., Festa, G., Bernard, P., Caracausi, A., Carluccio, I., Clinton, J. F., ... & Sokos, E.  
720 (2022). The Near Fault Observatory community in Europe: a new resource for faulting and hazard  
721 studies. *Annals of Geophysics*, 65(3), DM316.
- 722 Chiodini, G., Granieri, D., Avino, R., Caliro, S., Costa, A., Minopoli, C., & Vilardo, G. (2010).  
723 Non-volcanic CO<sub>2</sub> Earth degassing: Case of Mefite d'Ansanto (southern Apennines),  
724 Italy. *Geophysical Research Letters*, 37(11).
- 725 Cianetti, S., Bruni, R., Gaviano, S., Keir, D., Piccinini, D., Saccorotti, G., & Giunchi, C. (2021).  
726 Comparison of deep learning techniques for the investigation of a seismic sequence: An  
727 application to the 2019, Mw 4.5 Mugello (Italy) earthquake. *Journal of Geophysical Research:*  
728 *Solid Earth*, 126(12), e2021JB023405.
- 729 D'Agostino, N., Silverii, F., Amoroso, O., Convertito, V., Fiorillo, F., Ventafridda, G., & Zollo,  
730 A. (2018). Crustal deformation and seismicity modulated by groundwater recharge of karst  
731 aquifers. *Geophysical Research Letters*, 45(22), 12-253.
- 732 D'Agostino, N., Métois, M., Koci, R., Duni, L., Kuka, N., Ganas, A., Georgiev, A., Jouanne, F.,  
733 Kaludjerovic, N., & Kandić, R. (2020). Active crustal deformation and rotations in the

- 734 southwestern Balkans from continuous GPS measurements. *Earth and Planetary Science Letters*,  
735 539, 116246.
- 736 Daout, S., D'Agostino, N., Pathier, E., Socquet, A., Lavé, J., Doin, M.P., Riesner, M., & Benedetti,  
737 L. (2023) Along-strike variations of strain partitioning within the Apennines determined from  
738 large-scale multi-temporal InSAR analysis. *Tectonophysics*, 867, 230076, ISSN 0040-1951,  
739 <https://doi.org/10.1016/j.tecto.2023.230076>.
- 740 De Landro, G., Amoroso, O., Stabile, T. A., Matrullo, E., Lomax, A., & Zollo, A. (2015). High-  
741 precision differential earthquake location in 3-D models: evidence for a rheological barrier  
742 controlling the microseismicity at the Irpinia fault zone in southern Apennines. *Geophysical*  
743 *Supplements to the Monthly Notices of the Royal Astronomical Society*, 203(3), 1821-1831.
- 744 Deichmann, N. (2017). Theoretical basis for the observed break in ML/M w scaling between small  
745 and large earthquakes. *Bulletin of the Seismological Society of America*, 107(2), 505-520.
- 746 Deschamps, A., & King, G. C. P. (1983). The Campania-Lucania (southern Italy) earthquake of  
747 23 November 1980. *Earth and Planetary Science Letters*, 62(2), 296-304.
- 748 Edwards, B., Kraft, T., Cauzzi, C., Kästli, P., & Wiemer, S. (2015). Seismic monitoring and  
749 analysis of deep geothermal projects in St Gallen and Basel, Switzerland. *Geophysical Journal*  
750 *International*, 201(2), 1022-1039.
- 751 Festa, G., Adinolfi, G. M., Caruso, A., Colombelli, S., De Landro, G., Elia, L., ... & Zollo, A.  
752 (2021). Insights into mechanical properties of the 1980 Irpinia fault system from the analysis of a  
753 seismic sequence. *Geosciences*, 11(1), 28.
- 754 Gualandi, A., Nichele, C., Serpelloni, E., Chiaraluce, L., Anderlini, L., Latorre, D., ... & Avouac,  
755 J. P. (2017). Aseismic deformation associated with an earthquake swarm in the northern Apennines  
756 (Italy). *Geophysical Research Letters*, 44(15), 7706-7714.
- 757 Gulia, L., & Wiemer, S. (2019). Real-time discrimination of earthquake foreshocks and  
758 aftershocks. *Nature*, 574(7777), 193-199.
- 759 Hawthorne, J. C., & Bartlow, N. M. (2018). Observing and modeling the spectrum of a slow slip  
760 event. *Journal of Geophysical Research: Solid Earth*, 123(5), 4243-4265.

- 761 Herrmann, M., & Marzocchi, W. (2021). Inconsistencies and lurking pitfalls in the magnitude–  
762 frequency distribution of high-resolution earthquake catalogs. *Seismological Research*  
763 *Letters*, 92(2A), 909-922.
- 764 Herrmann, M., Piegari, E., & Marzocchi, W. (2022). Revealing the spatiotemporal complexity of  
765 the magnitude distribution and b-value during an earthquake sequence. *Nature*  
766 *Communications*, 13(1), 5087.
- 767 Hunter, J. D. (2007). Matplotlib: A 2D graphics environment. *Computing in science &*  
768 *engineering*, 9(03), 90-95. [Software]
- 769 Iannaccone, G., Zollo, A., Elia, L., Convertito, V., Satriano, C., Martino, C., Festa, G., Lancieri,  
770 M., Bobbio, A., Stabile, T. A., Vassallo, M. & Emolo, A., 2010. A prototype system for earthquake  
771 early-warning and alert management in southern Italy. *Bull. Earthq. Eng.*, 8(5), 11051129.
- 772 Improta, L., De Gori, P., & Chiarabba, C. (2014). New insights into crustal structure, Cenozoic  
773 magmatism, CO<sub>2</sub> degassing, and seismogenesis in the southern Apennines and Irpinia region from  
774 local earthquake tomography. *Journal of Geophysical Research: Solid Earth*, 119(11), 8283-8311.
- 775 Kaviris, G., Elias, P., Kapetanidis, V., Serpetsidaki, A., Karakonstantis, A., Plicka, V., ... &  
776 Bernard, P. (2021). The western Gulf of Corinth (Greece) 2020–2021 seismic crisis and cascading  
777 events: First results from the Corinth Rift Laboratory Network. *The Seismic Record*, 1(2), 85-95.
- 778 Keilis-Borok, V. (1959). On estimation of the displacement in an earthquake source and of source  
779 dimensions. *Annali di geofisica*, 12(2), 205-214.
- 780 Liu, F., Xue, S., Wu, J., Zhou, C., Hu, W., Paris, C., ... & Yu, P. S. (2020). Deep learning for  
781 community detection: progress, challenges and opportunities. *arXiv preprint arXiv:2005.08225*.
- 782 Lomax, A., Virieux, J., Volant, P., & Berge-Thierry, C. (2000). Probabilistic earthquake location  
783 in 3D and layered models: Introduction of a Metropolis-Gibbs method and comparison with linear  
784 locations. *Advances in seismic event location*, 101-134.
- 785 Lomax, A. (2020). Absolute location of 2019 Ridgecrest seismicity reveals a shallow Mw 7.1  
786 hypocenter, migrating and pulsing Mw 7.1 foreshocks, and duplex Mw 6.4 ruptures. *Bulletin of*  
787 *the Seismological Society of America*, 110(4), 1845-1858.
- 788 Madariaga, R. (1976). Dynamics of an expanding circular fault. *Bulletin of the Seismological*  
789 *Society of America*, 66(3), 639-666.

- 790 Mancini, S., Segou, M., Werner, M. J., Parsons, T., Beroza, G., & Chiaraluce, L. (2022). On the  
791 Use of High-Resolution and Deep-Learning Seismic Catalogs for Short-Term Earthquake  
792 Forecasts: Potential Benefits and Current Limitations. *Journal of Geophysical Research: Solid*  
793 *Earth*, 127(11), e2022JB025202.
- 794 Marshall, S. T., & Morris, A. C. (2012). Mechanics, slip behavior, and seismic potential of  
795 corrugated dip-slip faults. *Journal of Geophysical Research: Solid Earth*, 117(B3).
- 796 Marzocchi, W., Spassiani, I., Stallone, A., & Taroni, M. (2020). How to be fooled searching for  
797 significant variations of the b-value. *Geophysical Journal International*, 220(3), 1845-1856.
- 798 Matrullo, E., De Matteis, R., Satriano, C., Amoroso, O., & Zollo, A. (2013). An improved 1-D  
799 seismic velocity model for seismological studies in the Campania–Lucania region (Southern  
800 Italy). *Geophysical Journal International*, 195(1), 460-473.
- 801 Michele, M., Chiaraluce, L., Di Stefano, R., & Waldhauser, F. (2020). Fine-scale structure of the  
802 2016–2017 Central Italy seismic sequence from data recorded at the Italian National  
803 Network. *Journal of Geophysical Research: Solid Earth*, 125(4), e2019JB018440.
- 804 Mori, J., & Frankel, A. (1990). Source parameters for small events associated with the 1986 North  
805 Palm Springs, California, earthquake determined using empirical Green functions. *Bulletin of the*  
806 *Seismological Society of America*, 80(2), 278-295.
- 807 Mousavi, S. M., Ellsworth, W. L., Zhu, W., Chuang, L. Y., & Beroza, G. C. (2020). Earthquake  
808 transformer—an attentive deep-learning model for simultaneous earthquake detection and phase  
809 picking. *Nature communications*, 11(1), 3952.
- 810 Münchmeyer, J., Woollam, J., Rietbrock, A., Tilmann, F., Lange, D., Bornstein, T., ... & Soto, H.  
811 (2022). Which picker fits my data? A quantitative evaluation of deep learning based seismic  
812 pickers. *Journal of Geophysical Research: Solid Earth*, 127(1), e2021JB023499.
- 813 Okada, Y.(1992) Internal deformation due to shear and tensile faults in a half-space. *Bulletin of*  
814 *the Seismological Society of America*, 82 (2), 1018–1040.  
815 <https://doi.org/10.1785/BSSA0820021018>
- 816 Oth, A., Wenzel, F., & Radulian, M. (2007). Source parameters of intermediate-depth Vrancea  
817 (Romania) earthquakes from empirical Green's functions modeling. *Tectonophysics*, 438(1-4), 33-  
818 56.

- 819 Palo, M., Picozzi, M., De Landro, G., & Zollo, A. (2023). Microseismicity clustering and mechanic  
820 properties reveal fault segmentation in southern Italy. *Tectonophysics*, 856, 229849.
- 821 Park, Y., Mousavi, S. M., Zhu, W., Ellsworth, W. L., & Beroza, G. C. (2020). Machine-learning-  
822 based analysis of the Guy-Greenbrier, Arkansas earthquakes: A tale of two  
823 sequences. *Geophysical Research Letters*, 47(6), e2020GL087032.
- 824 Park, Y., Beroza, G. C., & Ellsworth, W. L. (2022). Basement fault activation before larger  
825 earthquakes in Oklahoma and Kansas. *The Seismic Record*, 2(3), 197-206.
- 826 Park, Y., Beroza, G. C., & Ellsworth, W. L. (2023). A mitigation strategy for the prediction  
827 inconsistency of neural phase pickers. *Seismological Society of America*, 94(3), 1603-1612.
- 828 Picozzi, M., Bindi, D., Festa, G., Cotton, F., Scala, A., & D'Agostino, N. (2022). Spatiotemporal  
829 evolution of microseismicity seismic source properties at the Irpinia Near-Fault Observatory,  
830 Southern Italy. *Bulletin of the Seismological Society of America*, 112(1), 226-242.
- 831 Poupinet, G., Ellsworth, W. L., & Frechet, J. (1984). Monitoring velocity variations in the crust  
832 using earthquake doublets: An application to the Calaveras Fault, California. *Journal of*  
833 *Geophysical Research: Solid Earth*, 89(B7), 5719-5731.
- 834 Prieto, G. A., Shearer, P. M., Vernon, F. L., & Kilb, D. (2004). Earthquake source scaling and self-  
835 similarity estimation from stacking P and S spectra. *Journal of Geophysical Research: Solid*  
836 *Earth*, 109(B8).
- 837 Resor, P. G., & Meer, V. E. (2009). Slip heterogeneity on a corrugated fault. *Earth and Planetary*  
838 *Science Letters*, 288(3-4), 483-491.
- 839 Ross, Z. E., Trugman, D. T., Hauksson, E., & Shearer, P. M. (2019). Searching for hidden  
840 earthquakes in Southern California. *Science*, 364(6442), 767-771.
- 841 Ross, Z. E., Cochran, E. S., Trugman, D. T., & Smith, J. D. (2020). 3D fault architecture controls  
842 the dynamism of earthquake swarms. *Science*, 368(6497), 1357-1361.
- 843 Rovida, A. N., Locati, M., Camassi, R. D., Lolli, B., & Gasperini, P. (2019). Catalogo parametrico  
844 dei terremoti italiani cpti15, versione 2.0.
- 845 Rubin, A. M., Gillard, D., & Got, J. L. (1999). Streaks of microearthquakes along creeping  
846 faults. *Nature*, 400(6745), 635-641.

- 847 Rubinstein, J. L., & Beroza, G. C. (2007). Full waveform earthquake location: Application to  
848 seismic streaks on the Calaveras fault, California. *Journal of Geophysical Research: Solid*  
849 *Earth*, *112*(B5).
- 850 Sagy, A., Brodsky, E. E., & Axen, G. J. (2007). Evolution of fault-surface roughness with  
851 slip. *Geology*, *35*(3), 283-286.
- 852 Schaff, D. P., Bokelmann, G. H., Ellsworth, W. L., Zanker, E., Waldhauser, F., & Beroza, G.  
853 C. (2004). Optimizing correlation techniques for improved earthquake location. *Bulletin of the*  
854 *Seismological Society of America*, *94*(2), 705-721.
- 855 Scholz, C. H. (2015). On the stress dependence of the earthquake b value. *Geophysical Research*  
856 *Letters*, *42*(5), 1399-1402.
- 857 Scotto di Uccio, F., Scala, A., Festa, G., Picozzi, M., & Beroza, G. C. (2023). Comparing and  
858 integrating artificial intelligence and similarity search detection techniques: application to seismic  
859 sequences in Southern Italy. *Geophysical Journal International*, *233*(2), 861-874.
- 860 Scotto di Uccio, F., & Festa, G. (2023). Catalog of relocated seismic sequences in Irpinia [Data  
861 set]. Zenodo. <https://doi.org/10.5281/zenodo.10441456>
- 862 Shearer, P. M. (2002). Parallel fault strands at 9-km depth resolved on the Imperial fault, southern  
863 California. *Geophysical Research Letters*, *29*(14), 19-1.
- 864 Silverii, F., D'Agostino, N., Borsa, A. A., Calcaterra, S., Gambino, P., Giuliani, R., & Mattone, M.  
865 (2019). Transient crustal deformation from karst aquifers hydrology in the Apennines  
866 (Italy). *Earth and Planetary Science Letters*, *506*, 23-37.
- 867 Simon, V., Kraft, T., Diehl, T., & Tormann, T. (2021). Possible Precursory Slow-Slip to Two ML ~  
868 3 Main events of the Diemtigen Microearthquake Sequence, Switzerland. *Geophysical Research*  
869 *Letters*, *48*(19), e2021GL093783.
- 870 Spallarossa, D., Cattaneo, M., Scafidi, D., Michele, M., Chiaraluce, L., Segou, M., & Main, I. G.  
871 (2021). An automatically generated high-resolution earthquake catalog for the 2016–2017 Central  
872 Italy seismic sequence, including P and S phase arrival times. *Geophysical Journal*  
873 *International*, *225*(1), 555-571.
- 874 Stabile, T. A., Satriano, C., Orefice, A., Festa, G., & Zollo, A. (2012). Anatomy of a  
875 microearthquake sequence on an active normal fault. *Scientific reports*, *2*(1), 410.

- 876 Stucchi, M., Meletti, C., Montaldo, V., Crowley, H., Calvi, G. M., & Boschi, E. (2011). Seismic  
877 hazard assessment (2003–2009) for the Italian building code. *Bulletin of the Seismological Society  
878 of America*, *101*(4), 1885-1911.
- 879 Sugan, M., Campanella, S., Chiaraluce, L., Michele, M., & Vuan, A. (2023). The unlocking  
880 process leading to the 2016 Central Italy seismic sequence. *Geophysical Research Letters*, *50*(5),  
881 e2022GL101838.
- 882 Supino, M., Festa, G., & Zollo, A. (2019). A probabilistic method for the estimation of earthquake  
883 source parameters from spectral inversion: application to the 2016–2017 Central Italy seismic  
884 sequence. *Geophysical Journal International*, *218*(2), 988-1007.
- 885 Supino, M., Poiata, N., Festa, G., Vilotte, J. P., Satriano, C., & Obara, K. (2020). Self-similarity  
886 of low-frequency earthquakes. *Scientific Reports*, *10*(1), 6523.
- 887 Tan, Y. J., Waldhauser, F., Ellsworth, W. L., Zhang, M., Zhu, W., Michele, M., ... & Segou, M.  
888 (2021). Machine-learning-based high-resolution earthquake catalog reveals how complex fault  
889 structures were activated during the 2016–2017 Central Italy sequence. *The Seismic Record*, *1*(1),  
890 11-19.
- 891 Trugman, D. T., & Shearer, P. M. (2017). GrowClust: A hierarchical clustering algorithm for  
892 relative earthquake relocation, with application to the Spanish Springs and Sheldon, Nevada,  
893 earthquake sequences. *Seismological Research Letters*, *88*(2A), 379-391.
- 894 Uieda, L., Tian, D., Leong, W. J., Toney, L., Schlitzer, W., Yao, J., Grund, M., Jones, M., 646  
895 Materna, K., Newton, T., Ziebarth, M., & Wessel, P. (2021). PyGMT: A Python 647 interface for  
896 the Generic Mapping Tools (v0.3.1) [Software]
- 897 Vassallo, M., Festa, G., Bobbio, A., & Serra, M. (2016). Low shear velocity in a normal fault  
898 system imaged by ambient noise cross correlation: The case of the Irpinia fault zone, Southern  
899 Italy. *Journal of Geophysical Research: Solid Earth*, *121*(6), 4290-4305.
- 900 Vuan, A., Sugan, M., Amati, G., & Kato, A. (2018). Improving the detection of low-magnitude  
901 seismicity preceding the Mw 6.3 L'Aquila earthquake: Development of a scalable code based on  
902 the cross correlation of template earthquakes. *Bulletin of the Seismological Society of  
903 America*, *108*(1), 471-480.

- 904 Vuan, A., Brondi, P., Sugan, M., Chiaraluce, L., Di Stefano, R., & Michele, M. (2020). Intermittent  
905 slip along the Alto Tiberina low-angle normal fault in central Italy. *Geophysical Research*  
906 *Letters*, *47*(17), e2020GL089039.
- 907 Waldhauser, F., & Ellsworth, W. L. (2000). A double-difference earthquake location algorithm:  
908 Method and application to the northern Hayward fault, California. *Bulletin of the seismological*  
909 *society of America*, *90*(6), 1353-1368.
- 910 Waldhauser, F. (2001). hypoDD--A program to compute double-difference hypocenter locations.
- 911 Waldhauser, F., Michele, M., Chiaraluce, L., Di Stefano, R., & Schaff, D. P. (2021). Fault planes,  
912 fault zone structure and detachment fragmentation resolved with high-precision aftershock  
913 locations of the 2016–2017 central Italy sequence. *Geophysical Research Letters*, *48*(16),  
914 e2021GL092918.
- 915 Westaway, R., & Jackson, J. (1987). The earthquake of 1980 November 23 in Campania—  
916 Basilicata (southern Italy). *Geophysical Journal International*, *90*(2), 375-443.
- 917 Yoon, C. E., Yoshimitsu, N., Ellsworth, W. L., & Beroza, G. C. (2019). Foreshocks and mainshock  
918 nucleation of the 1999 M w 7.1 Hector Mine, California, Earthquake. *Journal of Geophysical*  
919 *Research: Solid Earth*, *124*(2), 1569-1582.
- 920 Zhu, W., & Beroza, G. C. (2019). PhaseNet: A deep-neural-network-based seismic arrival-time  
921 picking method. *Geophysical Journal International*, *216*(1), 261-273.
- 922 Zollo, A., Orefice, A., & Convertito, V. (2014). Source parameter scaling and radiation efficiency  
923 of microearthquakes along the Irpinia fault zone in southern Apennines, Italy. *Journal of*  
924 *Geophysical Research: Solid Earth*, *119*(4), 3256-3275.

# 1 **Characterization and evolution of seismic sequences in the normal** 2 **fault environment of the Southern Apennines**

3  
4 *Francesco Scotto di Uccio*<sup>1</sup>, *Maddalena Michele*<sup>2</sup>, *Claudio Strumia*<sup>1</sup>, *Mariano Supino*<sup>2</sup>,  
5 *Gregory C. Beroza*<sup>3</sup>, *Lauro Chiaraluce*<sup>2</sup>, *Nicola D'Agostino*<sup>2</sup>, *Gaetano Festa*<sup>1,2</sup>

6  
7 <sup>1</sup> Department of Physics 'Ettore Pancini', University of Napoli Federico II, 80126 Napoli, Italy.

8 <sup>2</sup> Istituto Nazionale di Geofisica e Vulcanologia, Rome, Italy.

9 <sup>3</sup> Department of Geophysics, Stanford University, Stanford, CA 94305, USA.

10  
11  
12 Corresponding author: Francesco Scotto di Uccio ([francesco.scottodiuccio@unina.it](mailto:francesco.scottodiuccio@unina.it))

## 13 14 15 **Key Points:**

- 16 • Accurate earthquake location for enhanced catalogs unveils kilometeric scale structures  
17 where seismic sequences occur in Southern Apennines.
- 18 • Static stress transfer drives the evolution of these seismic sequences, with earthquakes  
19 dominantly distributed along the dip direction.
- 20 • Slip-dominated alignments of the seismicity could map the fault roughness or the boundary  
21 between locked and creeping domains.  
22

## 23 **Abstract**

24 The use of seismic catalogs enhanced through advanced detection techniques improves the  
25 understanding of earthquake processes by illuminating the geometry and mechanics of fault  
26 systems. In this study, we performed accurate hypocentral locations, source parameters estimation  
27 and stress release modelling from deep catalogs of microseismic sequences nucleating in the  
28 complex normal fault system of the Southern Apennines (Italy). The application of advanced  
29 location techniques resulted in the relocation of ~30% of the earthquakes in the enhanced catalogs,  
30 with relocated hypocenters clearly identifying local patches on kilometer-scale structures that  
31 feature consistent orientation with the main faults of the area. When mapping the stress change on  
32 the fault plane, the inter-event distance compared to the size of the events suggests that the  
33 dominant triggering mechanism within the sequences is static stress transfer. The distribution of  
34 events is not isotropic but dominantly aligned along the dip direction. These slip-dominated  
35 lineations could be associated with striations related to fault roughness and could map the  
36 boundary between locked and creeping domains in Apulian platform and basement.

## 37 **Plain Language Summary**

38 The development of earthquake detection techniques, based on machine learning or similarity, has  
39 allowed to increase seismic catalogs of more than one order of magnitude. However, how much  
40 information can be extracted from these small cracklings is still to be understood, especially in  
41 complex normal fault systems, such as the Apennine environment in Italy. For seismic sequences  
42 in Southern Apennines, we show that only a few portion (about 30%) of events in enhanced  
43 catalogs can be further characterized in terms of location and source properties. Nevertheless, the  
44 use of deep catalogs allows to illuminate kilometric scale structures at depths between 8 and 15  
45 km, to define mechanisms for seismicity evolution, mainly driven by static stress triggering, to  
46 identify seismicity alignments along the slip direction, eventually associated with fault roughness  
47 or delimiting boundaries between locked and creeping regions.

## 48 **1 Introduction**

49 Seismic sequences are comprised of earthquakes that are clustered in space and time and that occur  
50 at a higher rate than the background seismicity. They contain powerful information for  
51 investigating the geometry and mechanical state of faults that may generate large magnitude

52 earthquakes. In the case of a major event, accurate location of foreshocks and aftershocks can  
53 inform the rupture process from the preparation phase to the arrest by illuminating the structural  
54 complexity of the causative fault (e.g., Lomax 2020, Waldhauser et al. 2021). Most sequences,  
55 however, occur during the interseismic period between large earthquakes, at smaller space scales,  
56 and feature main events of low to moderate magnitude (Chiaraluce et al. 2009). These sequences  
57 can last from few days (Stabile et al. 2012, Scotto di Uccio et al. 2023) to months or years (Kaviris  
58 et al. 2021) and can provide insights into stress conditions at depth, potential asperities (Festa et  
59 al. 2021), fluid diffusion (Chen et al. 2012), aseismic processes (Gualandi et al. 2017), or other  
60 forcing mechanisms that can perturb the stress state in the brittle crust (Silverii et al., 2019).

61 Knowledge of structures and processes from the analysis of the sequences strongly depends on the  
62 content and the magnitude of completeness of available catalogs. Recently, enhanced catalogs  
63 obtained through advanced automatic detection techniques such as machine learning and  
64 similarity-based approaches (Chamberlain et al. 2018, Zhu & Beroza 2018, Mousavi et al. 2020,  
65 Liu et al. 2020, Spallarossa et al. 2021, Scotto di Uccio et al. 2023, Sukan et al. 2023) have  
66 contributed to increase the number of newly cataloged events by more than one order of magnitude,  
67 improving the magnitude of completeness by at least one magnitude unit. Machine learning based  
68 phase pickers have been shown to provide phase arrival times consistent with analyst  
69 identifications (Mousavi et al. 2020, Cianetti et al. 2021, Münchmeyer et al. 2022), even for  
70 earthquakes outside the regions used in the training datasets (e.g., Mousavi et al. 2020, Park et al.  
71 2020, Tan et al. 2021). Furthermore, event similarity can be exploited for closely spaced events  
72 using cross-correlation to measure P and S arrivals for smaller magnitude earthquakes from  
73 template events (Poupinet et al. 1984, Vuan et al. 2018, Chamberlain et al. 2018).

74 Phase picks can be used for precise earthquake location using differential location methods  
75 (Waldhauser & Ellsworth 2000, Trugman & Shearer 2017). However, hypocenter determination  
76 of low magnitude earthquakes in enhanced catalogs is challenging because these events typically  
77 emerge from the noise only at the few closest stations with uncertain arrival times. A typical  
78 percentage of template matched events that can be relatively located from enhanced catalogs is ~  
79 20% (Cabrera et al. 2022). Nevertheless, accurate locations from deep catalogs can provide a high-  
80 resolution image of fault structures, help to discern their interaction (e.g., Ross et al. 2019, Park et  
81 al. 2022, Sukan et al. 2023), and illuminate paths for possible fluid migration (Ross et al. 2020,  
82 Vuan et al. 2020).

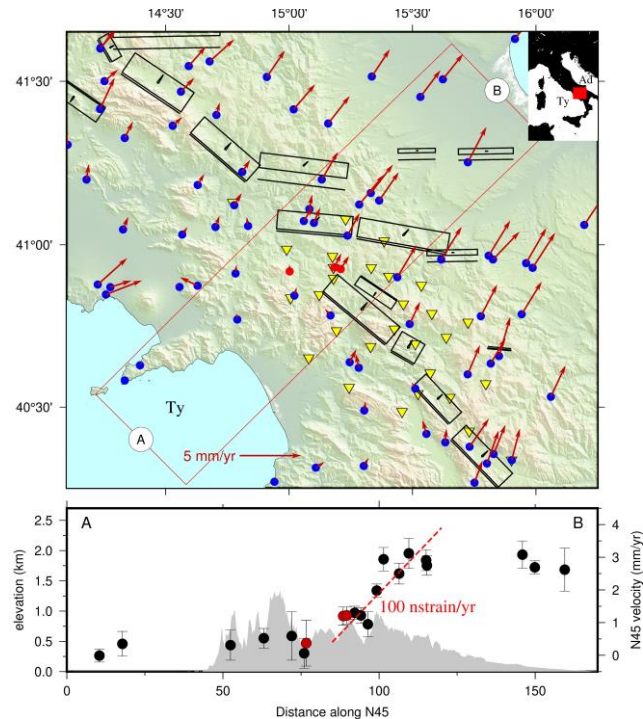
83 Deep catalogs can be statistically exploited in their space-time-magnitude evolution for inferring  
84 macroscopic physical processes to relate seismic sequences to background seismicity (Hermann  
85 et al. 2022, Scotto di Uccio et al. 2023), which may improve the predictability of short-term  
86 forecasting (Gulia & Wiemer 2019, Beroza et al. 2021). Reliable estimation of the frequency-  
87 magnitude characteristics of the catalogs requires a correct estimation of the event size and the  
88 catalog magnitude of completeness to avoid biases in b-value estimates (Marzocchi et al. 2020,  
89 Mancini et al. 2022).

90 Extracting physical constraints on the source process of events in deep catalogs is challenging due  
91 to the small signal-to-noise ratio and the narrow available frequency band. Local and moment  
92 magnitudes for small events can be estimated using time or frequency domain measurements (e.g.,  
93 Abercrombie 1995, Edwards et al. 2015, Hawthorne & Burtlow 2018, Supino et al. 2020, Scotto  
94 di Uccio et al. 2023). The source corner frequency (or event duration in time domain), which is a  
95 proxy for the earthquake size, can be obscured by anelastic attenuation effects (Deichmann, 2017)  
96 or the sampling rate (Abercrombie 2015). Several approaches have been proposed to reduce the  
97 correlation between the attenuation of the medium crossed by seismic waves and the source  
98 parameters. These are either based on the Empirical Green's function (EGFs) approach (Mori &  
99 Frankel 1990, Prieto et al. 2004), or based on the determination of attenuation relationships (Oth  
100 et al. 2007), which can allow a decrease in the minimum magnitude for which the source  
101 parameters can be estimated (Abercrombie 2015). While the use of EGFs is appealing in removing  
102 the propagation contribution, small events should be at least one point of magnitude smaller than  
103 the earthquake for most EGF approaches (Abercrombie & Rice 2005). EGF availability is often  
104 limited at the stations closest to the hypocenter, in a limited frequency band, where the signal  
105 emerges from the noise. When properly retrieving the source parameters for events in the sequence,  
106 they can help constrain the mechanisms associated with their evolution, e.g., whether they are  
107 triggered by stress release in cascade-like models or are driven by other forcing mechanisms (e.g.,  
108 Stabile et al. 2012, Yoon et al. 2019).

109 In this study we focused on seismic sequences in the Irpinia region, Southern Apennines (Italy).  
110 The area is one of the highest hazard regions of Italy (Stucchi et al. 2011) and experienced the  
111 most destructive seismic event in recent decades in that country. The 1980, M 6.9, Irpinia  
112 earthquake occurred on multiple, separate fault segments that were activated within 40s of the  
113 event origin (Figure 1), leading to more than 3000 casualties (Rovida et al. 2019). The region is

114 currently deforming, with a strain rate of  $\sim 100$  nstrain/yr corresponding to an increase of  $\sim 3$  mm/yr  
115 over 30 km across the axis of the Apennines (Daout et al., 2003; Figure 1). In the last 15 years, the  
116 area has been monitored by the Irpinia Near-Fault Observatory (INFO, triangles in Figure 1), with  
117 a dense seismic network of 31 stations equipped with accelerometers and short-period or broad-  
118 band seismometers (Iannaccone et al. 2010, Chiaraluce et al. 2022). Recent seismicity is  
119 characterized by low magnitude events (maximum magnitude 3.8), mainly occurring at depths  
120 between 8 and 15 km (De Landro et al. 2015), within the fault system that generated the 1980  
121 Irpinia earthquake and is mainly concentrated in a volume of low vs, high  $Q_p$ , high  $v_p/v_s$ , which  
122 suggests fluid-saturated conditions (Vassallo et al. 2016, Amoroso et al. 2017). Also, source  
123 parameters show a variability in the stress drop that could be modulated by fluid composition and  
124 concentration (Picozzi et al. 2021). In the area seismicity sometimes occurs clustered in seismic  
125 sequences that last several days, characterized by main events of magnitude lower than 3.5.  
126 Detailed studies of two sequences have shown a complex pattern for the seismicity and suggested  
127 that stress triggering can be the main driver of their evolution (Stabile et al. 2012, Festa et al.  
128 2021). Recently an enhanced catalog for 10 seismic sequences has been obtained for the area  
129 (Scotto di Uccio et al. 2023), built on the integration of machine learning and template matching,  
130 that increased the number of events relative to the existing manual catalog by a factor 7. In this  
131 study we seek to exploit the improved catalog to better understand the space-time evolution of the  
132 seismic sequences. We found that seismic sequences can be accurately located with uncertainties  
133 of  $\sim 100$  m, they occur on secondary structures with respect to the main segments of the 1980  
134 Irpinia earthquakes and their evolution appears to be mainly driven by static stress transfer.  
135 Preferential alignments of the seismicity along the dip direction might be an indication of  
136 simultaneous aseismic transients, especially for the most populated sequence.

137 First, we present the data used in the work (Section 2). Then, we describe the methods for  
138 accurately locating the events in the sequence, determining the source parameters and building a  
139 model to describe the stress release on the fault plane hosting the sequence (Section 3). Finally, we  
140 present the results obtained for the sequences, interpreting their spatio-temporal evolution (Section  
141 4), along with discussions and conclusions.



142 *Figure 1) Top panel: GPS velocity field in a Tyrrhenian reference frame. Yellow triangles indicate the seismic stations*  
 143 *of INFO. GPS stations SNAL, ANG1, and MTMR are displayed in red circles. The black boxes are the historical faults*  
 144 *that generated the largest earthquakes in the area, as reported by the Database of Individual Seismogenic Sources*  
 145 *(DISS, <https://seisnofaults.eu/services/diss-services>). Bottom panel: Elevation along the A-B section of top panel and*  
 146 *velocity field related to the GPS stations within the red box of top panel along the N45E direction. The study area is*  
 147 *currently accumulating strain at  $\sim 100$  nstrain/yr corresponding to an increase of  $\sim 3$  mm/yr across the axial part of*  
 148 *the Apennines.*

## 149 **2 Data**

150 In this work we characterized the spatio-temporal evolution of seismic sequences that occurred  
 151 near the Irpinia Near Fault Observatory. The sequences occurred between 2011 and 2020 and  
 152 featured main events of low to moderate local magnitude ( $1.8 < M_l < 3.7$ ). We selected the  
 153 enhanced catalogs obtained by Scotto di Uccio et al. (2023) using machine learning derived  
 154 detections (EQTransformer, Mousavi et al. 2020) as template sets for a further similarity-based  
 155 detection (EQCorrscan, Chamberlain et al. 2018). The integration of machine learning and  
 156 template matching has been shown to improve the manual catalogs by a factor  $\sim 7$  in this region.  
 157 The catalogs for the sequences obtained in Scotto di Uccio et al. (2023) feature an improved  
 158 magnitude of completeness of more than one magnitude unit and provide  $\sim 1.8$ k events, with nearly  
 159 800 events in the Rocca San Felice sequence.

160 We extended the initial phase-pick dataset to all the stations not included in the detection step in  
161 Scotto di Uccio et al. (2023). We used the velocity data when available, and the acceleration data  
162 as a second choice, following the same strategy used in Scotto di Uccio et al. (2023).

163 The cross-correlation delay times for double difference earthquake re-locations were evaluated on  
164 traces decimated to 100 Hz (Michele et al., 2020), obtained trimming raw continuous waveforms  
165 around the origin time from absolute locations. In the evaluation of source parameters for the  
166 relocated events, we pre-processed the raw traces by removing the instrumental response,  
167 including a 5% Hann taper and a water level regularization during the deconvolution stage. We  
168 bracketed the *S* wave window from 1 s before to 3 s after the phase arrival time. We considered  
169 the frequency band that satisfied the condition of SNR between the event and the noise spectra  
170 larger than 3.5 based on a comparison with a 4s time window before the event origin time.

## 171 **3 Methods**

### 172 **3.1 Absolute and relative locations**

173 For locating the earthquakes in the enhanced catalogs, we used available P and S arrival times. For  
174 template events, we obtained phase arrival times with the machine learning picker. The consistency  
175 between the automatic and manual picks was demonstrated in Scotto di Uccio et al. (2023), who  
176 found that the residuals featured zero mean values and a slightly larger dispersion for the S phase  
177 (standard deviation of 0.2 s). For the low magnitude events identified by the template matching,  
178 they performed cross-correlation (CC) picking and retained those measurements with a CC value  
179 of greater than 0.7. The consistency of template picks helps to ensure the reliability of the CC-  
180 derived phase arrival times. Moreover, the similarity-based detection step can add missed picks by  
181 machine learning picker, also for events with moderate signal-to-noise ratio (Park et al. 2023).  
182 When an arrival time was declared by both pickers, we selected the phase provided by the machine  
183 learning technique. Arrival time uncertainties are estimated by considering the associated  
184 probability for machine learning picks and the CC values for template matching phases,  
185 respectively. We converted the probability values (ranging between 0.1 and 1.0) into discrete  
186 weights for location (from 0 to 4, increasing numbers correspond to larger uncertainties) according  
187 to the table proposed by Mousavi et al. (2020). For the template matching picks, we imposed at  
188 least the same level of accuracy of the machine learning picks used for the declaration, eventually

189 increasing the discrete weights for low cross-correlation values. We raised the discrete weights by  
190 one point for every decimal of CC coefficient detaching from 1.0.

191 We estimated earthquake location using NonLinLoc (Lomax et al. 2000), which adopts a  
192 probabilistic approach to determine the location using the travel time residuals with statistically  
193 robust uncertainties. We tested three velocity models for the location procedure. Starting from a 1-  
194 D layered velocity model tailored for the Irpinia area (Matrullo et al. 2013), we derived two  
195 gradient models, which smooth the discontinuities in the wave velocity across layer boundaries,  
196 by linearly interpolating values between either the top or the middle points of the layers (Figure  
197 S1). We note that the velocity model obtained fixing the velocity value at the top of the layers  
198 systematically overestimates the velocity in each layer. The interpolated model obtained by fixing  
199 the velocity values at the centre of the layers resulted in lower location uncertainties, so we selected  
200 this model for event location. A few poorly constrained events result in an unreliable shallow  
201 location estimate; for these cases, we selected the location solutions obtained from the expected  
202 values of the probability density function (Lomax et al. 2000).

203 We used absolute locations as the starting point for relative re-locations of events in each sequence  
204 using HYPODD (Waldhauser & Ellsworth 2000), based on differential travel times for event pairs.  
205 For the evaluation of the catalog delay times in each sequence we used the picks for event pairs  
206 separated by less than 10 km in absolute location at all the available stations. For CC differential  
207 travel times, we evaluated the delay times for events that were separated by less than 10 km, on  
208 seismograms decimated to 100 Hz and filtered in the frequency band [1.5 – 15] Hz (Schaff et al.  
209 2004, Michele et al. 2020).

210 We assessed the length of the time windows for extracting the waveforms around the P and S  
211 arrival times by performing parametric tests. Too short windows resulted into too high values of  
212 CC coefficients such that the reliability of the lag measurement was overestimated. We selected a  
213 1.1 s (1.4 s) long window around the P (S) phase arrival time for calculating the CC coefficients,  
214 imposing a maximum lag of 1s. We only retained delay times for events with CC coefficient higher  
215 than 0.7.

216 We estimated relative locations with HYPODD using an iterative least square procedure (LSQR)  
217 that minimized the differential time residuals for pairs of earthquakes recorded at common stations  
218 by adjusting the vector connecting their hypocentres (Waldhauser & Ellsworth 2000). We used 4

219 steps of 4 iterations (a total of 16 iterations) of damped and dynamically weighted least square  
 220 inversions. In the initial settings, we assigned higher weights to catalog delay times, for better  
 221 constraining the location of the clusters, and we increased the contribution of the CC differential  
 222 travel times in the following settings, to consider the different position of the events within the  
 223 cluster. The damping factor was selected to stabilize the problem (Waldhauser 2001). To avoid  
 224 inconsistency with ray patterns used in the absolute locations, we extracted a 1-D model composed  
 225 of 20 thin layers from a resampling of the velocity model used in the absolute locations.

226 LSQR only approximates some aspects of the uncertainty (Waldhauser & Ellsworth 2000), so we  
 227 applied the Singular Value Decomposition (SVD) method for a more complete assessment of  
 228 location errors. The SVD option for double difference locations can only solve for a significantly  
 229 lower number of earthquakes than the LSQR option. Nevertheless, we were able to apply the SVD  
 230 technique for all the sequences apart from the Rocca San Felice sequence. For this latter sequence,  
 231 discussed in detail in the Section 4, we estimated location uncertainties using a bootstrap strategy.  
 232 We realized 200 independent double difference location runs on subsets of events within the  
 233 sequence. Each subset was obtained by randomly extracting 150 events, 60 % of which belong to  
 234 the machine learning catalog. This constraint in the selection of the events in each subset ensures  
 235 a more robust linkage to the cluster, since the number of picks associated with templates is  
 236 generally larger than for template-matched events. We evaluated the location uncertainties from a  
 237 statistical analysis based on the distance of each event from the cluster centroid for all the runs  
 238 where that event was located. This procedure allows quantification of the dependency of the results  
 239 on the single subset. For the  $i$  – th event we estimated the uncertainty along the  $j$  – th direction  
 240 as  $err_j^i = median_{(p,m)} |(x_{j,p}^i - x_{j,p}^c) - (x_{j,m}^i - x_{j,m}^c)|$ , where  $p$  and  $m$  indicate two  
 241 independent runs in which the  $i$  – th event was located, and the superscript  $c$  refers to the cluster  
 242 centroid of the considered run. The robustness of these estimates has been verified observing  
 243 agreement with uncertainties from a SVD inversion for the subset of template events.

### 244 **3.2 Source Parameters**

245 We used a probabilistic inversion approach (Supino et al., 2019) for retrieving earthquake source  
 246 parameters (seismic moment  $M_0$  and corner frequency  $f_c$ ) from the S-wave displacement  
 247 amplitude spectra of relocated events. This technique is grounded in a Bayesian inversion of the

248 spectra and allows an exploration of the correlations among parameters with a robust estimation  
 249 of the uncertainties. The source is described by a generalized Brune model (Brune, 1970)

$$\tilde{S}(M_0, f_c, \gamma; f) = \frac{M_0}{1 + \left(\frac{f}{f_c}\right)^\gamma} \quad (1)$$

250 where the spectral fall-off at high-frequencies  $\gamma$  is considered as free parameter. The propagation  
 251 contribution is described by the term (e.g., Supino et al. 2019)

$$\tilde{G}(Q, f) = KAe^{-\pi fT/Q} \quad (2)$$

252 where  $T$  is the source-receiver travel-time,  $Q$  is the quality factor related to anelastic attenuation,  
 253  $A$  is the geometrical spreading (assumed as  $1/r$ , where  $r$  is the source-receiver distance) and

$$K = \frac{R_S F}{4\pi\rho\beta^3} \quad (3)$$

254 We assumed the average radiation pattern for S-waves  $R_S = 0.63$  (Boore & Boatwright 1984), a  
 255 free surface reflection coefficient of  $F = 2$ , the density  $\rho = 2700 \text{ kg/m}^3$  and the S-wave velocity  
 256  $\beta = 3027 \text{ m/s}$  (Zollo et al. 2014). After removing the instrumental response, the displacement  
 257 amplitude spectrum can be written as:

$$\tilde{U}(M_0, f_c, \gamma, Q; f) = \tilde{S}(M_0, f_c, \gamma; f) \cdot \tilde{G}(Q; f) \quad (4)$$

258 The modelling of the spectra requires a joint inversion for source parameters and quality factor,  
 259 which are strongly correlated. To reduce this correlation, we tried to evaluate the quality factor  
 260 separately from the inversion of source parameters. We started by considering the small events in  
 261 each sequence as empirical Green's functions (EGF). For those events the effective (source) corner  
 262 frequency is much larger than the apparent corner frequency of the anelastic attenuation low-pass  
 263 filter, and sometimes even larger than the Nyquist frequency of the records (in this case  $f_{Nyq} =$   
 264  $62.5 \text{ Hz}$ ). Considering the EGF spectra in the domain where  $f \ll f_c$ , the displacement spectrum  
 265 can be approximated as:

$$\tilde{U}_{EGF} = KAM_0 e^{-\pi fT/Q_{EGF}} \quad (5)$$

266 We selected events featuring local magnitude  $M_l < 1$  as EGFs and fit with a linear model  $\log \tilde{U}_{EGF}$   
 267 as a function of the frequency to retrieve  $M_0$  and  $Q_{EGF}$ . The frequency band selected for the fit

268 respects the constraint of a signal-to-noise ratio larger than 3.5 for each frequency in the band. The  
 269 value of  $Q_{EGF}$  is station dependent.

270 Since events in the same sequence share almost the same source-receiver path, we expect a  
 271 consistency in the  $Q_{EGF}$  estimates across the EGFs for the same station. For stations presenting at  
 272 least 5 estimates of  $Q_{EGF}$ , we evaluated the compatibility of the inferred values and used the mean  
 273 value to correct for anelastic attenuation.

274 For other stations, for which we have insufficient high-quality EGFs, we attempted to estimate a  
 275 sequence-dependent quality factor  $Q_{LOC}$  by exploring different values of the anelastic attenuation  
 276 around the average regional estimate  $Q_{REG} = 230$  (Zollo et al., 2014). Considering events with  
 277  $Ml > 1$ , we inverted the displacement amplitude spectra, and fixed the attenuation to one of the  
 278 following values  $Q = 100, 170, 230, 300, 400$  in different inversion runs. We compared the  
 279 average residuals resulting from the best solution for the source parameters in each run. We  
 280 selected as  $Q_{LOC}$  the  $Q$  value producing the lowest misfit, imposing a minimum number of 5  
 281 solutions per station. We finally kept  $Q = Q_{REG}$  for stations where neither  $Q_{EGF}$  nor  $Q_{LOC}$  could be  
 282 evaluated.

283 Finally, the inversion technique provided the seismic moment  $M_0$  (and the moment magnitude  $M_w$ )  
 284 for all the events, but corner frequencies only for events with  $Ml > 1$ . Quality of the solutions was  
 285 checked by analysing the shape of the a-posteriori probability density function related to the  
 286 estimated parameters. Solutions not showing peaked probability functions were discarded  
 287 following the strategy defined in Supino et al. (2019).

### 288 **3.3 Stress change model**

289 For events in the sequence for which we estimated both moment magnitude and corner frequency,  
 290 we computed the source radius  $a$  as (Madariaga, 1976):

$$a = k \frac{\beta}{f_c} \quad (6)$$

291 where  $k$  is a geometrical shape factor, which was assumed here as  $k = 0.37$  (Brune, 1970). We  
 292 derived the stress drop  $\Delta\sigma$  from seismic moment and the source radius (Keilis-Borok 1959) as:

$$\Delta\sigma = \frac{7}{16} \frac{M_0}{a^3} \quad (7)$$

293 We then evaluated the average stress drop  $\Delta\bar{\sigma}$  for the sequence as the mean value of the retrieved  
294 stress drops. We associated the average stress drop  $\Delta\bar{\sigma}$  with all other events in the sequence for  
295 which we were not able to estimate the corner frequency, and we used the above relationship to  
296 retrieve the event source radius.

297 We evaluated the rupture plane associated with the seismic sequence as the best-fit plane across  
298 the hypocenters of the events in the sequence. If the locations did not constrain a plane, we used  
299 the focal mechanism solutions from Palo et al. (2023) and selected the plane that is more consistent  
300 with the expected orientation of faults in the area. We finally mapped the stress change on the fault  
301 plane associated with the sequence, using the rupture model proposed by Andrews (1980) and a  
302 non-isotropic representation of the stiffness. Since in the rupture model neither the slip nor the  
303 stress drop is considered constant, we imposed the condition that the average stress drop within  
304 the crack from the Andrews model coincided with the event stress drop computed from the source  
305 parameters.

#### 306 **4 Results**

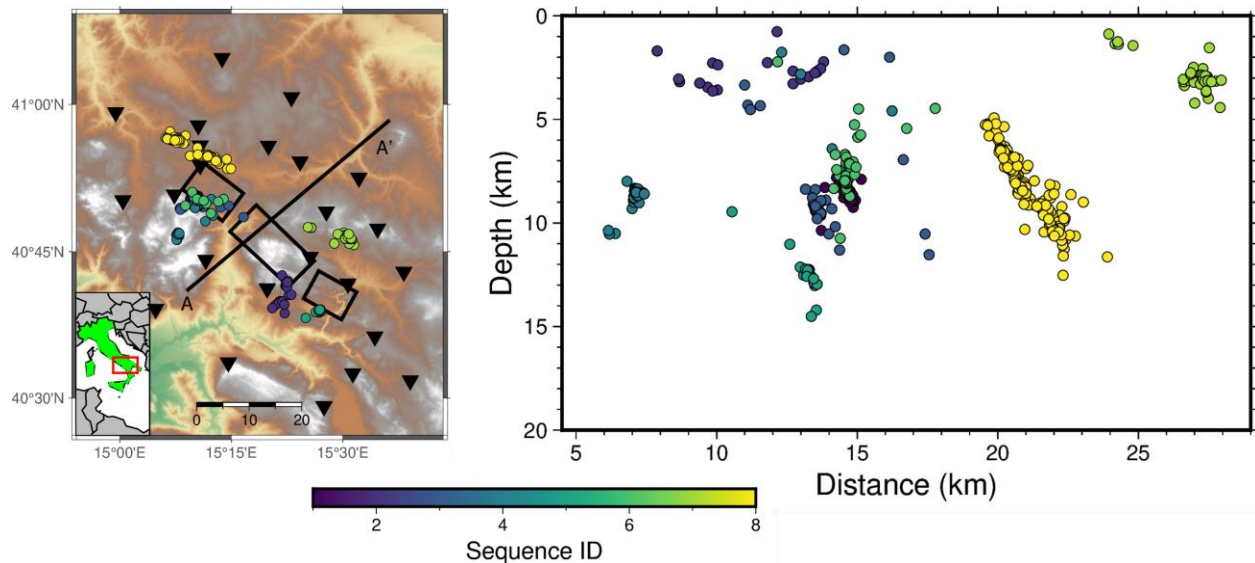
307 For all the enhanced catalogs related to the sequences in Scotto di Uccio et al. (2023), we computed  
308 absolute and (double difference) relative locations using NonLinLoc and HYPODD codes. Using  
309 the automatic phase arrival times provided by the integration of machine learning and template  
310 matching pickers, we obtained absolute locations for 1130 events ( $\sim 60\%$  of the detection catalog).  
311 The uncertainties can be as large as few kilometers, resulting into several tenths of second root-  
312 mean square (RMS) of travel time residuals. This uncertainty is enough to obscure the fault  
313 segments or patches on which the seismicity takes place. The number of absolute locations from  
314 the enhanced catalogs is 5 times larger than in the manual INFO bulletin and provides a wide set  
315 of catalog and cross-correlation delay times for earthquake relocation. When analyzing the single  
316 sequences, the improvement in the number of located earthquakes ranges from a factor 2.5 to 8.5.

317 Starting from the absolute positions of earthquakes in the enhanced catalogs, we achieved double  
318 difference relocation of 550 events total, from 8 out of the 10 seismic sequences analyzed in Scotto  
319 di Uccio et al. (2023). The two sequences for which we did not get relocations (IDX 7 and IDX 9

320 in Scotto di Uccio et al. 2023) feature the lowest number of detections (about 40 events). The total  
 321 number of relocated events represents  $\sim 30\%$  of the enhanced catalog. A similar fraction is  
 322 observed for each of the relocated sequences and results coherent with earthquake relocation of  
 323 other template matching derived catalogs (Cabrera et al. 2022, Ross et al. 2019), due to low signal-  
 324 to-noise ratio of small events leading to limited pick availability and triggered stations.

325 Figure 2 shows the double difference relocation of the earthquakes in the enhanced catalogs. In  
 326 the left panel we show the position of epicenters with respect to the seismic network. In the right  
 327 panel the hypocenters are projected along the vertical plane A-A' oriented perpendicular to the  
 328 trend of the Apennines (N40°E). This plane represents the direction orthogonal to the main  
 329 structures of the area, that generated the 1980 Irpinia earthquake. In Table S1 we report the label  
 330 of the sequences in this work with respect to the references in Scotto di Uccio et al. (2023).

331



332

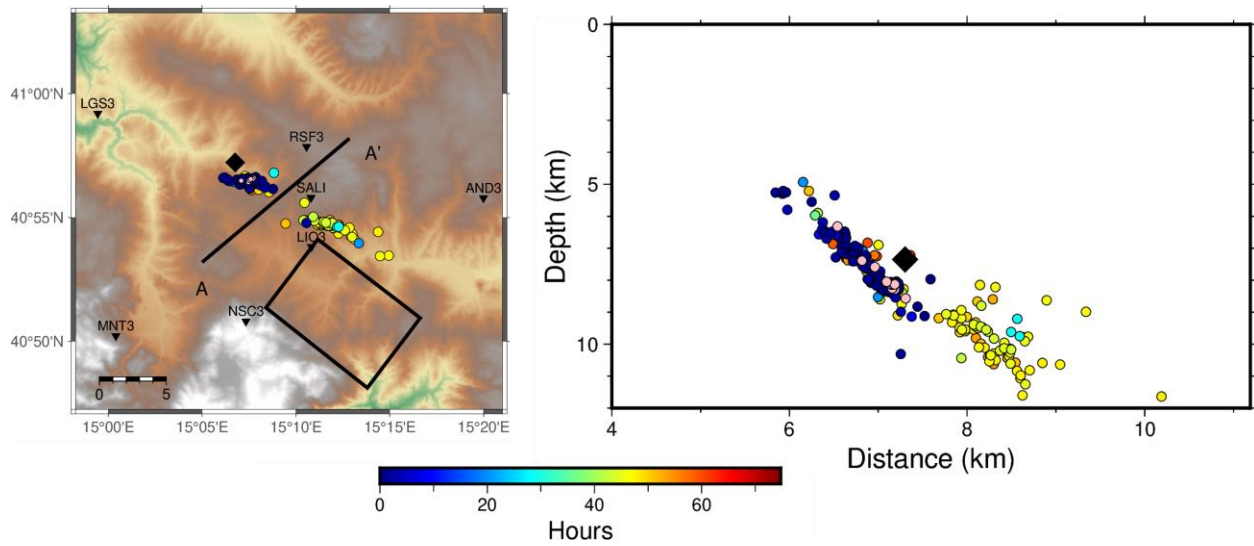
333 *Figure 2) Left panel: Epicentral location for the relocated events, colored according to the sequence IDX and*  
 334 *representation of the fault traces in the Irpinia area. Stations are shown with black triangles. Right panel: Cross-*  
 335 *section along the A-A' vertical plane, orthogonal to the main structure of the 1980 M6.9 earthquake for which rupture*  
 336 *planes are shown with black rectangles.*

337 The cross-section shows that the seismicity patterns feature clear alignments and a high degree of  
 338 clustering, highlighting km-sized structures that share similar dips. For all sequences, the spatial  
 339 extent of the sequences depicted by relocations is much greater than what expected from the total  
 340 released seismic moment.

341 The Rocca San Felice sequence, marked in Figure 2 with yellow dots (IDX 8) features the highest  
342 number of both detections and double difference located events ( $\sim 800$  and 250 events  
343 respectively). For this sequence, we were able to estimate absolute locations for about 60 % of the  
344 detections, with average horizontal and depth uncertainties of 1.5 km (average RMS residuals of  
345 0.4 s). We evaluated double difference relocations, limiting the analysis to events with at least 2  
346 P-picks and one S-pick among the three stations closest to the centroid of the sequence ( $\sim 300$   
347 located earthquakes). From about 97.5 k catalog differential times (47k for P phase, 50.5k for S  
348 phase) and 85k CC delay times (31k for P phase, 54k for S phase) we obtained a catalog of 250  
349 relocated events with median location uncertainties of 91 m, 31 m and 105 m in the East, North  
350 and vertical directions, respectively. When zooming on the sequence location (Figure 3 - left  
351 panel), the position of the epicenters clearly suggests the presence of two clusters, at 5 km of  
352 distance from each other. The projection of the seismicity along the vertical plane oriented  $N40^\circ E$   
353 (Figure 3 – right panel), indicates that the two clusters feature similar orientations but occurred at  
354 different depths: the shallower one is mostly confined between 6 km and 9 km, the deeper one  
355 between 9.5 km and 11 km. The two clusters were activated at different times during the sequence,  
356 as shown in Figure 3, where the colors denote the occurrence time of the events relative to the  
357 mainshock. The events occurred within the first two days of the mainshock illuminate a first 4-km  
358 long segment with a dip of  $55^\circ$ , coherently with the focal mechanism estimated by Festa et al.  
359 (2021). Two days after the main event, the occurrence of a  $M_l$  2.8 event activated a deeper  
360 secondary patch of slightly shorter extent with a similar orientation.

361 The presence of two separated clusters was not recognized in the previous work of Festa et al.  
362 (2021) and is supported by the change in the first station recording the P wave arrival, that occurred  
363 at the station RSF3 for events in the first cluster and at LIO3 for events in the second one. In Figure  
364 S2 we reported the vertical records, at the closest stations, for two events belonging to the two  
365 clusters. It is worth to note that the improvement in double difference location as compared to the  
366 results of Festa et al. (2021) comes from the combination of a deeper event catalog, but also from  
367 a larger number of picks per event. Indeed, for most of the events we were able to retrieve picks  
368 and waveforms also for the accelerometric station SALI, located close to the centroid epicenter,  
369 indicating that strong motion sensors can provide useful information even for microseismic events  
370 if their sensitivity is high enough (for SALI it is  $4.0 \text{ V/m/s}^2$ ).

371



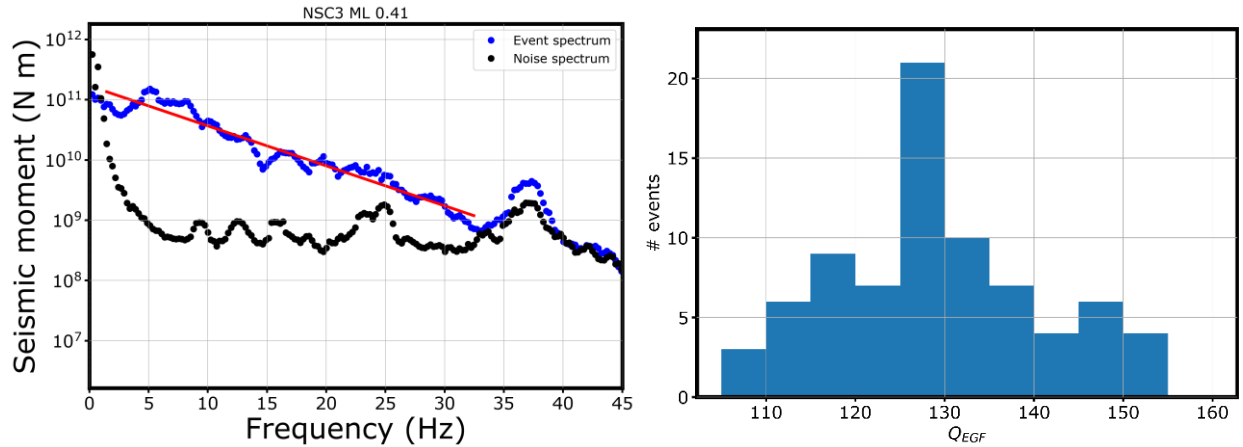
372

373 *Figure 3) Left panel: Spatio-temporal evolution of the epicenters for the Rocca San Felice seismic sequence (IDX 8),*  
 374 *colored according to the occurrence time from the main event. Foreshocks are represented with pink circles and the*  
 375 *main event is represented with a black diamond. Right panel: Cross-section along the vertical plane as in Figure 2,*  
 376 *colored according to the occurrence time from the main event.*

377 We inverted the displacement spectra of the relocated events to infer the seismic moment  $M_0$  (and  
 378 hence the moment magnitude  $M_w$ ), the corner frequency  $f_c$  and the quality factor  $Q$  as output. For  
 379 each sequence, we separated events with local magnitude above and below 1.0, according to the  
 380 estimates of Scotto di Uccio et al. (2023) as described in Section 2. We then estimated  $M_0$  and  $Q$   
 381 for the events in the sequence below the magnitude threshold, considered as EGFs, and used these  
 382 parameters to infer the moment and the corner frequency of the larger events (above the threshold).

383 Here, we illustrate all the steps in our analysis for the Rocca San Felice sequence, which we also  
 384 applied to all the other sequences. For the stations closest to the sequence, recording many small  
 385 magnitude events ( $M_l < 1$ ), we tried to estimate the quality factor  $Q_{EGF}$  by fitting the logarithm  
 386 of the displacement spectra as a linear function of the frequency. For each EGF, we perform the fit  
 387 in the frequency band where the signal-to-noise ratio exceeds the threshold of 3.5. As an example,  
 388 we show in Figure 4 - left panel- the displacement amplitude spectrum and the corresponding noise  
 389 spectrum for a  $M_l 0.41 \pm 0.10$  earthquake at the station NSC3 ( $\sim 11$  km distance from the main  
 390 event). We estimated the quality factor for the considered earthquake from the slope of the linear  
 391 fit (Figure 4, left panel), whose intercept is proportional to the seismic moment. We thus estimated

392 the quality factor  $Q_{EGF}$  from the fit of each candidate EGF. An example of  $Q_{EGF}$  distribution (for  
 393 the station NSC3) is reported in the right panel of Figure 4. We observe a peaked Gaussian-like  
 394 distribution, which is typical of stations providing a large number of estimates for the quality  
 395 factor. We extracted the weighted mean of individual  $Q_{EGF}$  values using the inverse of the fit  
 396 residuals as weighting factors, to describe the quality factor  $\bar{Q}_{EGF}$  for that station-sequence couple.



397

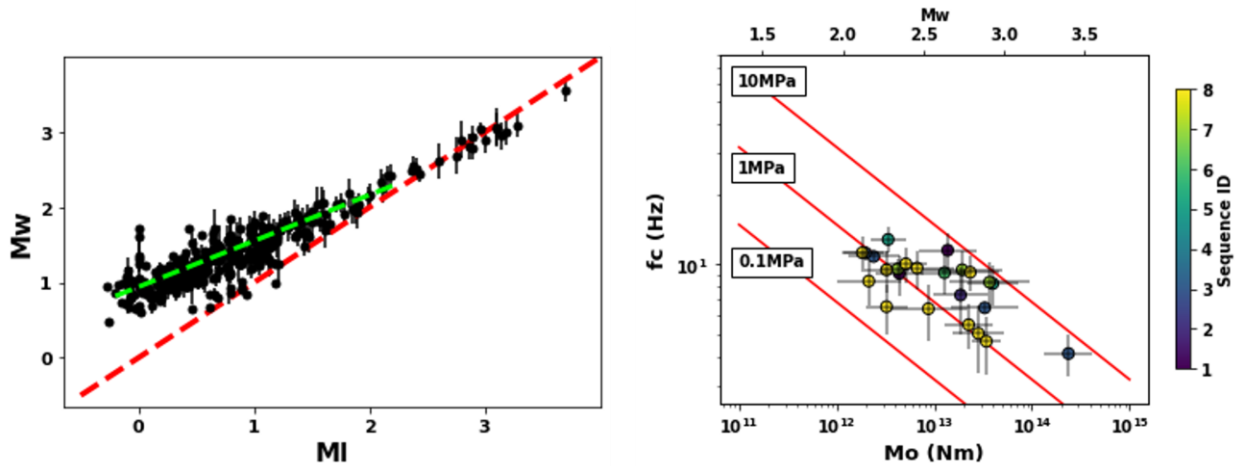
398 *Figure 4) Left panel:  $Q_{EGF}$  estimation from linear fit (red solid line) of the logarithm of the displacement event spectrum*  
 399 *(blue dots) as a function of the linear frequency, for a  $M_l = 0.41$  earthquake. Noise spectrum is reported as black*  
 400 *dots. Right panel: histogram of the  $Q_{EGF}$  for the events  $M_l < 1$  in the Rocca San Felice sequence (IDX 8) at NSC3*  
 401 *station*

402 For the example of Figure 4, we estimated  $\bar{Q}_{EGF} = 130 \pm 12$  for NSC3, which is smaller than  
 403 the regional estimation provided by Zollo et al. (2014).

404 For the stations lacking sufficient high-quality EGFs, we attempted to extract a local quality factor  
 405  $Q_{LOC}$  by performing several inversions with different, fixed  $Q_s$  values. We then assumed as the  
 406 most suitable value of  $Q$  the one that resulted in the lowest average RMS residuals. In the case of  
 407 the Rocca San Felice sequence, this procedure allowed estimation of the quality factor for five  
 408 stations (COL3, SCL3, SFL3, SNR3, SSB3). For stations where neither  $Q_{EGF}$  nor  $Q_{LOC}$  was  
 409 estimated, we considered the regional value of the area for the quality factor ( $Q_s = 230$ , Zollo et  
 410 al. 2014). After the estimation of the quality factor from the EGF, we attempted to estimate the  
 411 source parameters for events with  $M_l > 1$ , by fitting the spectra with the generalized Brune model.  
 412 In Figure S3 we report the fit results for a  $M_l = 2.8$  event at three stations. In Figure S3 – left panel  
 413 – we represent the fit of the displacement spectrum at the station NSC3, where we used an EGF

414 derived quality factor ( $Q_{EGF} = 130$ ). In the central panel we report the results for the station SCL3  
 415 ( $\sim 43$  km from the main event) where we estimated a quality factor  $Q_{LOC} = 300$ , higher than the  
 416 average estimate for the area. We note that in this latter case, the average value ( $Q = 230$ ) provides  
 417 unreliaibly large corner frequencies (as compared to the values obtained at other stations), close to  
 418 the upper limit of the frequency band used for the inversion. In the right panel, we show the fit for  
 419 the station VDS3 ( $\sim 38$  km from the main event), for which we used the regional value  $Q_{REG} =$   
 420 230.

421 For the Rocca San Felice seismic sequence, we retrieved the seismic moment  $M_0$  for 45 % of the  
 422 located events, while we globally estimated the seismic moment for 236 out of the 550 relocated  
 423 events ( $\sim 60\%$ ). In Figure 5 - left panel we report the distribution of the moment magnitude  $M_w$   
 424 (Hanks and Kanamori, 1979), against the local magnitude  $M_l$ , as evaluated in Scotto di Uccio et  
 425 al. (2023), considering all the events for which an estimation of the seismic moment was available.  
 426 The red line marks the 1:1 trend between  $M_l$  and  $M_w$ .



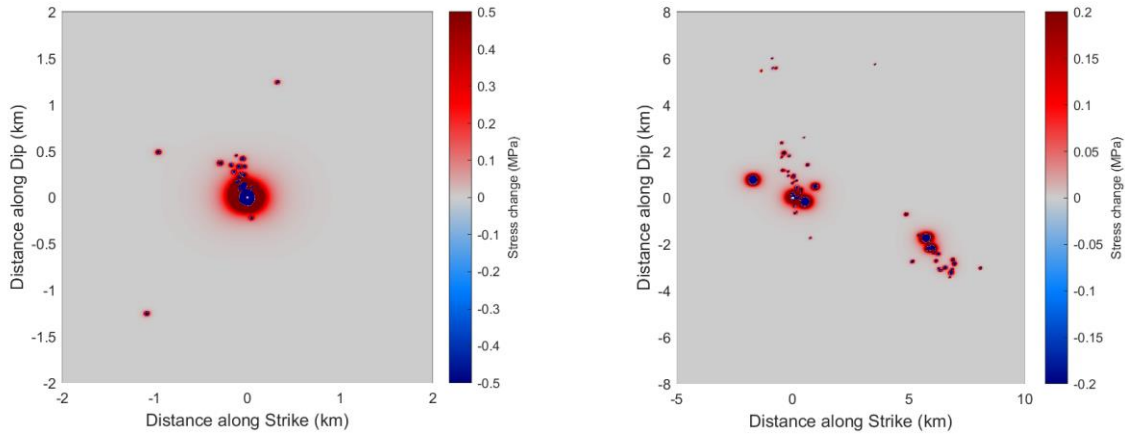
427  
 428 *Figure 5) Left panel:  $M_w - M_l$  distribution, with the 1:1 relation scaling reported as dashed red line. For  $M_l < 2$*   
 429 *earthquakes, we observed  $M_w = 0.89 (\pm 0.03) + 0.62 (\pm 0.02)M_l$  (green dashed line). Right panel: Distribution of*  
 430 *source parameters for  $M_w > 2$ , colored according to sequence IDX, with theoretical constant stress drops scaling of*  
 431 *0.1 MPa, 1 MPa and 10 MPa (red solid lines)*

432 We recognize two trends between the magnitude scales: for  $M_l < 2$  the distribution strongly  
 433 deviates from the 1:1 scaling relation. Evaluating the average value of  $M_w$  in different  $M_l$  bins of  
 434 width 0.2 and performing a linear fit between the two quantities, we retrieved  $M_w = a + b * M_l =$   
 435  $0.89 (\pm 0.03) + 0.62 (\pm 0.02)M_l$  (the linear fit curve is reported with a green dashed line). The

436 estimated slope agrees with the predictions of Deichmann (2017), which indicated a saturation of  
437 the event duration in the local magnitude computation due to the anelastic attenuation, resulting  
438 into the scaling  $M_w = C + \frac{2}{3} M_l$ . For  $M_l > 2$ , the distribution follows the 1:1 scaling trend  
439 between  $M_l$  and  $M_w$ , as also found by Zollo et al. (2014). In the right panel of Figure 5 we reported  
440 the  $\log M_0 - \log f_c$  distribution, with red straight lines marking the theoretical trends obtained  
441 assuming characteristic stress drop values of  $\Delta\sigma = 100kPa, 1MPa$  and  $10 MPa$ . The single  
442 station corner frequencies have been averaged considering the relative uncertainty of the estimate.  
443 As a result, we determined seismic moment and corner frequency for events with moment  
444 magnitude  $M_w > 2.0$ , while for events below this magnitude, the solution for the corner frequency  
445 was not constrained (Supino et al. 2019). For the resolved events, the distribution of the corner  
446 frequencies with moment appears to follow a nearly linear trend, with stress drop ranging between  
447 1-3 MPa. For the Rocca San Felice sequence, yellow marks in the right panel of Figure 5, the  
448 average  $\Delta\sigma$  resulted to be  $\sim 1.0 MPa$

449 We evaluated the source size for all the events for which we estimated the seismic moment, either  
450 by considering the retrieved corner frequency or by assuming self-similarity. The former condition  
451 applies to the largest magnitude events in the sequences, the latter for lower magnitude events. For  
452 each sequence, we assessed the best fitting plane from earthquake locations, and represented the  
453 static stress released by single events onto this plane (Andrews et al. 1980) along the strike and  
454 dip directions. For almost all the sequences (IDXs 1 to 7) the stress model suggests static stress  
455 release as a trigger mechanism, with small events mainly concentrated in or around the area  
456 affected by stress changes due to the main events in the sequence. As an example, we report in  
457 Figure 6 – left panel - the stress release model for a seismic sequence featuring a  $M_l$  2.9 main event  
458 (IDX 1 in Figure 2). We observe a single km-sized patch mainly oriented along the dip direction,  
459 with earthquakes occurring within the volume interested by the main event. We retrieved similar  
460 dip – oriented trends also for the other considered sequences. An interesting case is represented by  
461 the Rocca San Felice seismic sequence (IDX 8 in Figure 2 and in Figure 3), illustrated in the right  
462 panel of Figure 6. For this sequence, we observe two seismicity patterns activated at different times  
463 (the main event  $M_l$  3.0 involved the leftmost patch, and the seismicity migrated along the rightmost  
464 segment almost two days after the mainshock with the occurrence of a  $M_l$  2.8 earthquake). In both

465 clusters we still observe a predominant orientation along the dip direction. In the following  
 466 discussion, we investigate the mechanical connection between these two patches.



467  
 468 *Figure 6) Stress released model for the IDX 1 (left panel) and IDX 8 (Rocca San Felice, right panel) sequence. In both*  
 469 *representations, we observe earthquakes occurring within the volume interested by the main event, with preferentially*  
 470 *dip-oriented patches.*

## 471 **5 Discussion**

472 Catalog enhancement using advanced detection techniques allows an increase in the number of  
 473 earthquakes up to an order of magnitude as compared to ordinary seismic catalogs. For seismic  
 474 sequences in the normal fault system of Southern Apennines (Italy), we find an enhancement of a  
 475 factor  $\sim 7$  with respect to the number of earthquakes manually detected by network operators  
 476 (Scotto di Uccio et al. 2023). The improvement in the magnitude of completeness of these deep  
 477 catalogs makes it possible to monitor variations in the statistical parameters describing the  
 478 seismicity, such as the b-value of the Gutenberg-Richter relation (Beroza et al. 2021). These  
 479 changes can only be roughly indicative of variations in the mechanical properties underlying the  
 480 faults, such as the differential stress (Scholz 2015); however, the evaluation and the consequent  
 481 use of these parameters for interpreting the evolution of the sequences is still debated, in part due  
 482 to biases in the magnitude estimates (Gulia & Wiemer 2019, Hermann & Marzocchi 2021, Mancini  
 483 et al. 2022).

484 The clearer view of the manifestation of the mechanical properties of structures in the form of  
 485 earthquake sequences can be achieved through accurate location and source parameter estimation;  
 486 however, the generally low signal-to-noise ratio of the new events in the enhanced catalogs, does

487 not fully translate into an equal increase in the number of earthquakes that can be accurately  
488 located. For seismic sequences in Irpinia, we retrieved double difference locations for  $\sim 30\%$   
489 events, a fraction similar or slightly larger than the percentage resulting from template matching  
490 derived catalogs (Ross et al. 2019, Simon et al. 2021, Cabrera et al. 2022). This reduction in the  
491 number of well-located events is driven by the different impact of the waveform similarity during  
492 the detection and the location phases. Template matching detection algorithms leverage on stacked  
493 cross-correlations across the entire network (Chamberlain et al. 2018, Vuan et al. 2018), resulting  
494 in a global similarity value, to which stations with both high and low cross-correlation values  
495 contribute. High-quality thresholds on the similarity coefficient for cross-correlation differential  
496 travel times requested by accurate double difference locations (Michele et al. 2020, Waldhauser et  
497 al. 2021), limit the number of available stations, especially for low magnitude events. Although  
498 the catalog of events located with double differences is only twice larger than the manual catalog,  
499 the improvement in cluster definition and spatial resolution is much more significant, allowing the  
500 identification of alignments and structures at kilometric scale, that were not clearly illuminated  
501 from the manual catalog (Palo et al. 2023), owing to the wide increase in the number of differential  
502 travel-times. As an example, for the Rocca San Felice sequence, we reported more than one order  
503 of magnitude more differential travel-times compared to the ones extracted from the manual  
504 catalog (Festa et al. 2021).

505 When moving to the moment magnitude estimation, the number of events in the enhanced catalog  
506 that can be characterized further decreases, to 15% of the detections (or 60% of the relocated  
507 events). Furthermore, we resolved the corner frequencies only for events with moment magnitude  
508  $M_w > 2.0$  already present in the network catalog due to the limited available frequency bandwidth  
509 for the inversion related to the signal-to-noise ratio and data sampling rate. Nevertheless, we were  
510 able to reduce the epistemic uncertainty in the estimate of source parameters due to the  
511 propagation, using small earthquakes as empirical Green's functions.

512 Averaging over all sequences, we found an average stress drop of  $\Delta\sigma = 2.35 \text{ MPa}$ ; its variability  
513 across sequences, estimated by the standard deviation is  $s_{\Delta\sigma} = 0.87 \text{ MPa}$ . The stress drop found  
514 here is one order of magnitude larger than the stress drop retrieved for the background seismicity  
515 in the area by Zollo et al. (2014), who used a similar inversion strategy and an independent catalog  
516 not influenced by the sequences studied here. Since they derived the average stress drop using the

517 Madariaga model (Madariaga 1976), when converting that value into an equivalent Brune's stress  
518 drop, they obtained a median value of  $\Delta\sigma = 0.26 \text{ MPa}$ . This difference indicates that the release  
519 of stress during sequences likely occurs in more compact asperities that can be associated with a  
520 higher coupling than for background seismicity (Chen & Shearer 2012).

521 The stress drops we retrieved for these seismic sequences are comparable to the estimate of  
522  $3.5 \text{ MPa}$ , achieved for the 1980, M 6.9 Irpinia earthquake (Deschamps & King 1983, Bernard &  
523 Zollo 1989). When mapping the seismic sequences at depth, their location is generally not  
524 compatible with faults that hosted the 1980 event - based on either the fault trace at the surface  
525 (Westaway & Jackson 1987) or the event dip and geometry estimated from seismic and levelling  
526 data (Bernard and Zollo 1989, Amoroso et al. 2005). This indicates that seismic sequences ruptured  
527 small patches of secondary segments, as compared to the main structure of the M 6.9 earthquake.

528 The investigated area undergoes a strain-rate of  $\sim 100 \text{ nstrain/yr}$  and an increase of  $3 \text{ mm/yr}$  over  
529  $30 \text{ km}$  along the axial sector of the Apennines. All the investigated sequences fall within the  
530 actively deforming area, providing important insight into the geometry of structures potentially  
531 activated during larger magnitude events. The Rocca San Felice sequence, roughly aligned along  
532 the northwestward continuation of the complex multi-segment fault system activated during the M  
533 6.9 earthquake, illuminates a NE-dipping structure whose geometry is favorably oriented for  
534 seismic release of NE-SW accumulated interseismic strain (Figure 1). This structure is not mapped  
535 in the catalog of the Italian seismogenic Faults (DISS, <https://diss.ingv.it/>), which should motivate  
536 additional investigation of the long-term, seismogenic behavior of the structures illuminated by  
537 local seismic sequences.

538 We found differences in the stress drops associated with sequences, with an increase of the stress  
539 drop moving from North to South in the Irpinia region, as also shown by Picozzi et al. (2022),  
540 whose catalog contains all the events with magnitude larger than 1.5 for the area. We found average  
541 stress drops of  $\Delta\sigma_N = 2.0 \text{ MPa}$  in the Northern sector (Cervialto Fault area, the initial rupturing  
542 segment of the 1980 earthquake) and  $\Delta\sigma_S = 2.8 \text{ MPa}$  in the Southern Sector (San Gregorio  
543 Magno Fault area, i.e., on the second rupturing segment of the 1980 earthquake). Tomographic  
544 images in velocity (Amoroso et al. 2014, Improta et al. 2014, Vassallo et al. 2016) and anelastic  
545 attenuation ( $Q_p$ ,  $Q_s$ ; Amoroso et al. 2017) coupled with rock physics modelling indicate the  
546 presence of pressurized fluids in the area of microseismicity. Differences in the stress drops

547 between the two areas could be associated with the different fluid content and fraction. In the  
548 Southern sector rock physics modelling indicates the presence of a mixture brine-CO<sub>2</sub> (Amoroso  
549 et al. 2017). The large, extended low V<sub>p</sub>/V<sub>s</sub> anomaly in tomographic images in the northern sector  
550 indicates a pressurized reservoir of fluids, associated with the large natural emission of low-  
551 temperature CO<sub>2</sub> at the Mefite d'Ansanto, Rocca San Felice site (Chiodini et al. 2010).

552 Several studies in the area indicate a correlation between shallow stress changes in the karst aquifer  
553 induced by hydrological loading via the poroelastic response of the rocks and deep seismicity  
554 (D'Agostino et al. 2018). Although most of the sequences occurred during the maximum aquifer  
555 charge, we cannot infer a clear link between stress changes in the shallow water table and the  
556 occurrence of the sequences. However, the small amount of stress perturbation that propagates at  
557 depth (D'Agostino et al., 2018) compared to the large stress drops retrieved during sequences may  
558 indicate an elastic coupling between the shallow Mesozoic carbonates and the underlying Apulian  
559 platform beneath the *mélange*, and a critical state of these small patches, that are prone to generate  
560 the sequences with a stress excess that is only a few percent of the stress drop required to nucleate  
561 events.

562 When mapping the stress change on the fault plane associated with the sequences, most of the  
563 events appear connected, indicating that the sequences ruptured single patches along the fault  
564 plane. The inter-event distance, compared to the size of the events, suggests that the dominant  
565 triggering mechanism within the sequences is static stress transfer, that allows the nucleation of  
566 individual events in the sequence. Nevertheless, an important feature retrieved here is that the  
567 distribution of the events is not isotropic around the main events of the sequences, but small events  
568 tend to align dominantly along the dip direction, which also corresponds to the slip direction, for  
569 normal faults. Specific patterns for sequences along the direction of the slip have been observed  
570 in strike-slip environments (Rubin et al. 1999, Shearer 2002). Lineation of the seismicity along the  
571 major faults in California have been interpreted as the boundary between locked and creeping  
572 domains (Rubin et al. 1999, Rubinstein and Beroza 2007). In the normal fault environment of  
573 Southern Apennines also, evolution of the seismicity during the sequences is controlled by slip and  
574 cannot be explained by the anisotropic stress release after the event (Andrews 1980, see also the  
575 stress changes of Figure 6). Fault roughness, modulated by repeated stick slip episodes may  
576 determine predominant patterns at the scale of the microseismicity observed here (10 – 100m),

577 with striations mainly oriented along the dip direction (Candela et al. 2011). Corrugated faults  
578 behave as geometrical asperities and can localize deformation hosting stick-slip episodes at small  
579 scales (few centimeters of slip) (Resor and Meer 2009). Fault roughness and geometrical barriers  
580 at this scale may also impede small events from growing into larger magnitude earthquakes (Sagy  
581 et al. 2007, Marshall and Morris 2012). These strips can also favor upward migration of fluids,  
582 although we cannot discern a signature of diffusion-dominated processes from the space-time  
583 evolution of the sequences.

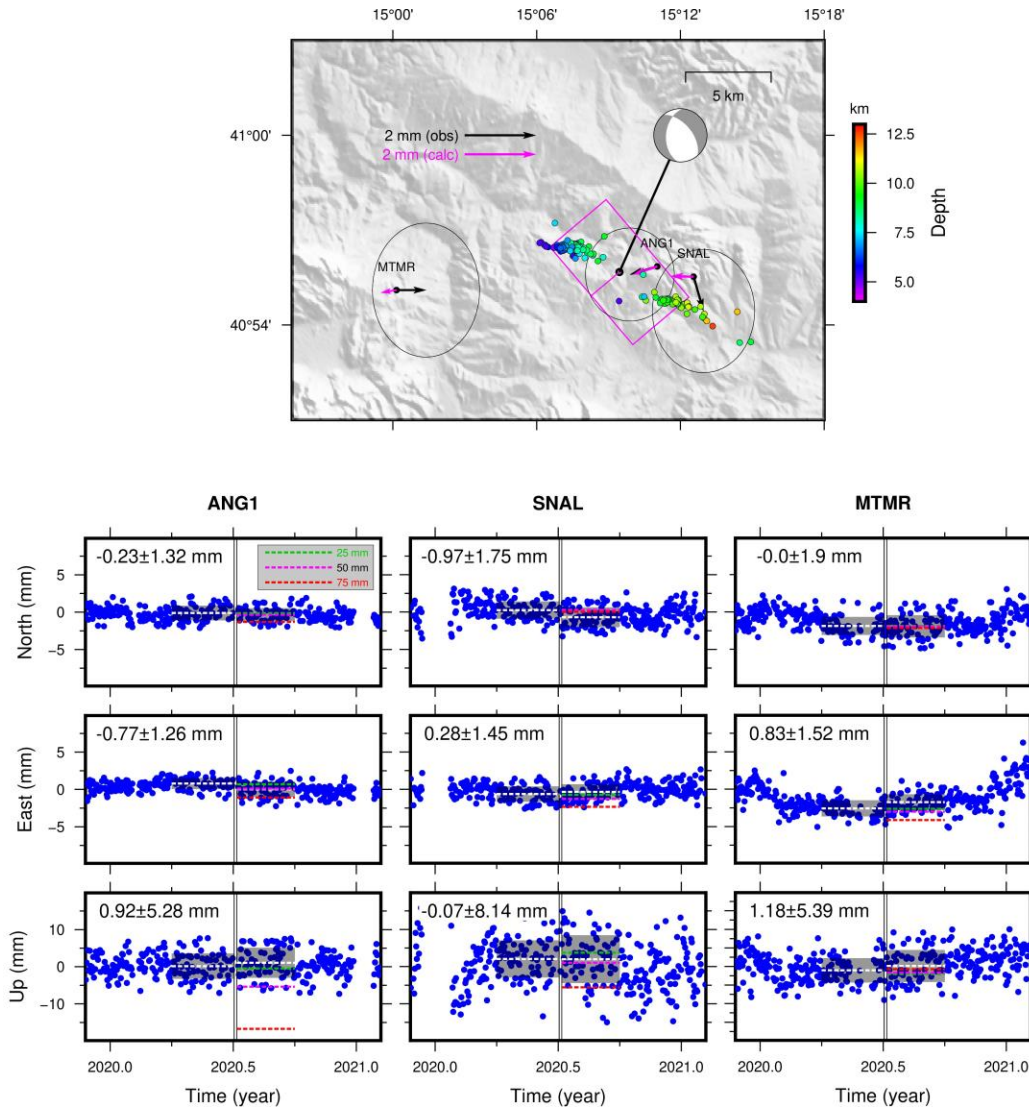
584 The occurrence of aseismic slip episodes nearby the lineations could also be the cause for the  
585 along-dip evolution of the seismicity and might explain the longer extent compared to the released  
586 seismic moment. Aseismic transients have been already observed in normal fault environments  
587 during the occurrence of larger seismic sequences (Gualandi et al. 2017, Kaviris et al. 2021).  
588 However, for the sequences analyzed here, geodetic data has not detected aseismic transients at  
589 this space-time scale during the sequences analyzed in this study.

590 The Rocca San Felice sequence shows the activation of two parallel clusters, oriented along the  
591 dip direction, but about 5 km apart. The two clusters featured main events of similar magnitude  
592 ( $M_l$  3.0 and  $M_l$  2.8, respectively), a kilometeric size extension along the dip (4 km and 2 km), with  
593 the first evolving preferentially up-dip, the second one downdip. The second cluster was activated  
594 about two days after the first sequence. As shown in Figure 6, the stress perturbation associated  
595 with the first sequence cannot be responsible for the activation of the second patch. Also, the lack  
596 of seismicity between the two segments does not support the hypothesis of fluid migration as  
597 responsible for triggering the second cluster. According to the rate of occurrence of independent  
598 events with  $M_l > 2.5$  in the northern part of the region ( $\lambda = 2.1 * 10^{-3} ev/day$ ), we estimated  
599 the probability of occurrence of two independent events within 2 days as about 0.4%.

600 We also tested the hypothesis of aseismic slip between the two seismicity clusters of this sequence.  
601 We assess the evolution of the displacement at the three closest GPS stations SNAL, MTMR,  
602 ANG1, the first two belonging to the INGV-RING network, the latter to the Regione Campania.  
603 The time series of daily coordinates (see D'Agostino et al., 2020 for details of GPS data  
604 processing) at the three stations have been checked for possible offsets across the seismic  
605 sequence. Evaluating the average positions in North, East and vertical coordinates, before and after

606 the Rocca San Felice sequence, we could not find significant static offsets within the estimated  
 607 error (Figure 7).

608



609 *Figure 7) Upper panel: map of the GPS stations near the Rocca San Felice seismic sequence and associated*  
 610 *displacements. The vectors show the horizontal displacements with one sigma error ellipses, from the static offset*  
 611 *during the seismic sequence. Circles represent events of the sequence color-coded with depth. Three different synthetic*  
 612 *scenarios were evaluated assuming increasing slip (25, 50, 75 mm), with geometry and kinematics from Festa et al.,*  
 613 *2021. The surface displacements produced by a slip of 50 mm on the fault drawn with purple lines is shown in the*  
 614 *map (purple arrows). Lower panel. GPS position time series and average positions (white dashed lines) before and*  
 615 *after the seismic sequence, with 1-sigma error shown with grey shading. Calculated displacements are also shown*  
 616 *(dashed lines) for the 25mm (green), 50mm (purple) and 75 mm (red) dislocation scenarios.*

617

618 We assessed the maximum average slip allowed on a deep dislocation whose displacement on the  
619 surface would not emerge from the noise level at the three GPS stations. We centered the potential  
620 aseismic dislocation between the two clusters and used the fault geometry and kinematics inferred  
621 by the composite focal mechanism solution of Festa et al. (2021) and calculated the surface  
622 displacements using the Okada techniques (Okada 1992). We tested a range of uniform slip on the  
623 dislocation between 25 and 75 mm, assuming constant strain drop of  $10^{-5}$ . The relatively deep  
624 position of the dislocation centroid between the two clusters ( $\sim 8$  km) allows slip on the deep  
625 dislocations up to 50 mm without detection at the surface (Figure 7). For slip larger than 50 mm  
626 the non-linear increase of cumulative seismic moment determines surface displacements outside  
627 the range of allowed offsets. Thus, an aseismic event of  $M_w \sim 5.0$  could have occurred during the  
628 sequence, transferring stress across the two asperities without producing a signal that would have  
629 been visible at the GPS stations.

## 630 **6 Conclusions**

631 In this work we presented a comprehensive analysis of seismic sequences through accurate  
632 earthquake location and source parameters estimation of enhanced catalogs (Scotto di Uccio et al.  
633 2023). Selecting machine learning and cross-correlation phase arrival times, we retrieved double  
634 difference locations for  $\sim 30\%$  of the events. The relocated seismicity revealed that seismic  
635 sequences involve kilometeric-scale structures, featuring a NW-SE dip and larger extent than  
636 expected from the magnitude of the mainshocks. While location of microseismicity usually relies  
637 on the use of records from velocimetric sensors, in this work the resolution of hypocenters  
638 benefited from phase arrival times determined on accelerometers located close to the main events  
639 of the sequences. Accelerometers can thus provide important arrival time information that is  
640 comparable in quality to velocimetric stations, improving the location results. For the relocated  
641 earthquakes, we estimated the source parameters (seismic moment  $M_0$ , corner frequency  $f_c$ )  
642 through a probabilistic inversion of the displacement spectra (Supino et al. 2019), and the resulting  
643 source size  $r$  and stress drop  $\Delta\sigma$ , assuming the generalized Brune model, finally mapping the stress  
644 change along the fault plane. We estimated the moment magnitude for 60% of the relocated events  
645 and we resolved the corner frequencies only for earthquakes with  $M_w > 2.0$ , using low-magnitude  
646 events as EGFs. We observed  $\Delta\sigma$  spanning the range  $[0.9 - 5.4]$  MPa, within the interval proposed  
647 for earthquakes in the Irpinia area (Picozzi et al. 2021) and source radius for the main events varies

648 from 105 – 235 m. We observed differences in the stress drops associated with sequences, with an  
649 increase of the stress drop from North to South in the Irpinia region, likely associated to the  
650 different fluid content and fraction. When mapping the stress change on the fault plane associated  
651 with the sequences, most of the events appear connected, indicating that the sequences ruptured  
652 single, contiguous patches along the fault plane. The inter-event distance, compared to the size of  
653 the events, suggests that the dominant triggering mechanism within the sequences is the (static)  
654 stress transfer, that allows the nucleation of individual events in the sequence. Alignment of events  
655 mainly along the dip direction indicates a slip dominated mechanism in the evolution of the  
656 seismicity, which could be associated with different fault roughness in the directions of the dip and  
657 strikes. Lineations in the definition of the seismicity might indicate aseismic transients occurring  
658 at the same time of the sequences. These transients could explain the migration of the seismicity  
659 from one cluster to the other one during the Rocca San Felice sequence. Although GPS data from  
660 stations located just above the sequence do not contain offsets indicative of such transients, a Mw  
661 5 aseismic event could have occurred at the sequence depth, without producing a signal emerging  
662 from the noise.

### 663 **Open Research**

664 Seismic products from the Irpinia Near Fault Observatory can be accessed through the Irpinia  
665 Seismic Network website (<https://isnet.unina.it>). Seismic data from INFO can be accessed through  
666 EIDA portal (<https://eida.ingv.it/it/>), network code IX or via the EPOS portal ([https://www.ics-](https://www.ics-c.epos-eu.org/)  
667 [c.epos-eu.org/](https://www.ics-c.epos-eu.org/)). GNSS data are accessible through the INGV website  
668 <ftp://bancadati2.gm.ingv.it:2121/OUTGOING/RINEX30/RING/>. Earthquake relocations were  
669 performed using NonLinLoc (<https://github.com/alomax/NonLinLoc>) and HYPODD  
670 (<https://www.ldeo.columbia.edu/~felixw/hypoDD.html>). Catalogs of the analyzed events are  
671 available at the following link: <https://zenodo.org/records/10441456> (Scotto di Uccio & Festa,  
672 2023) Maps in Figure 2 and Figure 3 were made using PyGMT (Uieda et al., 2021). Figure 4 and  
673 Figure 5 were produced using Matplotlib (Hunter, J.D., 2007). Figure 6 was produced using  
674 Matlab.

675

676

677 **References**

- 678 Abercrombie, R. E., & Rice, J. R. (2005). Can observations of earthquake scaling constrain slip  
679 weakening?. *Geophysical Journal International*, *162*(2), 406-424.
- 680 Abercrombie, R. E. (2015). Investigating uncertainties in empirical Green's function analysis of  
681 earthquake source parameters. *Journal of Geophysical Research: Solid Earth*, *120*(6), 4263-4277.
- 682 Abercrombie, R. E. (1995). Earthquake source scaling relationships from -1 to 5 ML using  
683 seismograms recorded at 2.5-km depth. *Journal of Geophysical Research: Solid Earth*, *100*(B12),  
684 24015-24036.
- 685 Amoroso, O., Ascione, A., Mazzoli, S., Virieux, J., & Zollo, A. (2014). Seismic imaging of a fluid  
686 storage in the actively extending Apennine mountain belt, southern Italy. *Geophysical Research  
687 Letters*, *41*(11), 3802-3809.
- 688 Amoroso, O., Russo, G., De Landro, G., Zollo, A., Garambois, S., Mazzoli, S., ... & Virieux, J.  
689 (2017). From velocity and attenuation tomography to rock physical modeling: Inferences on fluid-  
690 driven earthquake processes at the Irpinia fault system in southern Italy. *Geophysical Research  
691 Letters*, *44*(13), 6752-6760.
- 692 Amoruso, A., Crescentini, L., D'Anastasio, E., & De Martini, P. M. (2005). Clues of postseismic  
693 relaxation for the 1915 Fucino earthquake (central Italy) from modeling of leveling  
694 data. *Geophysical Research Letters*, *32*(22).
- 695 Andrews, D. J. (1980). A stochastic fault model: 1. Static case. *Journal of Geophysical Research:  
696 Solid Earth*, *85*(B7), 3867-3877.
- 697 Bernard, P., & Zollo, A. (1989). The Irpinia (Italy) 1980 earthquake: detailed analysis of a complex  
698 normal faulting. *Journal of Geophysical Research: Solid Earth*, *94*(B2), 1631-1647.
- 699 Beroza, G. C., Segou, M., & Mostafa Mousavi, S. (2021). Machine learning and earthquake  
700 forecasting—next steps. *Nature communications*, *12*(1), 4761.
- 701 Boore, D. M., & Boatwright, J. (1984). Average body-wave radiation coefficients. *Bulletin of the  
702 Seismological Society of America*, *74*(5), 1615-1621.
- 703 Brune, J. N. (1970). Tectonic stress and the spectra of seismic shear waves from  
704 earthquakes. *Journal of geophysical research*, *75*(26), 4997-5009.

- 705 Cabrera, L., Poli, P., & Frank, W. B. (2022). Tracking the spatio-temporal evolution of foreshocks  
706 preceding the Mw 6.1 2009 L'Aquila earthquake. *Journal of Geophysical Research: Solid*  
707 *Earth*, 127(3), e2021JB023888.
- 708 Candela, T., Renard, F., Schmittbuhl, J., Bouchon, M., & Brodsky, E. E. (2011). Fault slip  
709 distribution and fault roughness. *Geophysical Journal International*, 187(2), 959-968.
- 710 Chamberlain, C. J., Hopp, C. J., Boese, C. M., Warren-Smith, E., Chambers, D., Chu, S. X., ... &  
711 Townend, J. (2018). EQcorrscan: Repeating and near-repeating earthquake detection and analysis  
712 in Python. *Seismological Research Letters*, 89(1), 173-181.
- 713 Chen, X., Shearer, P. M., & Abercrombie, R. E. (2012). Spatial migration of earthquakes within  
714 seismic clusters in Southern California: Evidence for fluid diffusion. *Journal of Geophysical*  
715 *Research: Solid Earth*, 117(B4).
- 716 Chiaraluce, L., Valoroso, L., Anselmi, M., Bagh, S., & Chiarabba, C. (2009). A decade of passive  
717 seismic monitoring experiments with local networks in four Italian  
718 regions. *Tectonophysics*, 476(1-2), 85-98.
- 719 Chiaraluce, L., Festa, G., Bernard, P., Caracausi, A., Carluccio, I., Clinton, J. F., ... & Sokos, E.  
720 (2022). The Near Fault Observatory community in Europe: a new resource for faulting and hazard  
721 studies. *Annals of Geophysics*, 65(3), DM316.
- 722 Chiodini, G., Granieri, D., Avino, R., Caliro, S., Costa, A., Minopoli, C., & Vilardo, G. (2010).  
723 Non-volcanic CO<sub>2</sub> Earth degassing: Case of Mefite d'Ansanto (southern Apennines),  
724 Italy. *Geophysical Research Letters*, 37(11).
- 725 Cianetti, S., Bruni, R., Gaviano, S., Keir, D., Piccinini, D., Saccorotti, G., & Giunchi, C. (2021).  
726 Comparison of deep learning techniques for the investigation of a seismic sequence: An  
727 application to the 2019, Mw 4.5 Mugello (Italy) earthquake. *Journal of Geophysical Research:*  
728 *Solid Earth*, 126(12), e2021JB023405.
- 729 D'Agostino, N., Silverii, F., Amoroso, O., Convertito, V., Fiorillo, F., Ventafridda, G., & Zollo,  
730 A. (2018). Crustal deformation and seismicity modulated by groundwater recharge of karst  
731 aquifers. *Geophysical Research Letters*, 45(22), 12-253.
- 732 D'Agostino, N., Métois, M., Koci, R., Duni, L., Kuka, N., Ganas, A., Georgiev, A., Jouanne, F.,  
733 Kaludjerovic, N., & Kandić, R. (2020). Active crustal deformation and rotations in the

- 734 southwestern Balkans from continuous GPS measurements. *Earth and Planetary Science Letters*,  
735 539, 116246.
- 736 Daout, S., D'Agostino, N., Pathier, E., Socquet, A., Lavé, J., Doin, M.P., Riesner, M., & Benedetti,  
737 L. (2023) Along-strike variations of strain partitioning within the Apennines determined from  
738 large-scale multi-temporal InSAR analysis. *Tectonophysics*, 867, 230076, ISSN 0040-1951,  
739 <https://doi.org/10.1016/j.tecto.2023.230076>.
- 740 De Landro, G., Amoroso, O., Stabile, T. A., Matrullo, E., Lomax, A., & Zollo, A. (2015). High-  
741 precision differential earthquake location in 3-D models: evidence for a rheological barrier  
742 controlling the microseismicity at the Irpinia fault zone in southern Apennines. *Geophysical*  
743 *Supplements to the Monthly Notices of the Royal Astronomical Society*, 203(3), 1821-1831.
- 744 Deichmann, N. (2017). Theoretical basis for the observed break in ML/M w scaling between small  
745 and large earthquakes. *Bulletin of the Seismological Society of America*, 107(2), 505-520.
- 746 Deschamps, A., & King, G. C. P. (1983). The Campania-Lucania (southern Italy) earthquake of  
747 23 November 1980. *Earth and Planetary Science Letters*, 62(2), 296-304.
- 748 Edwards, B., Kraft, T., Cauzzi, C., Kästli, P., & Wiemer, S. (2015). Seismic monitoring and  
749 analysis of deep geothermal projects in St Gallen and Basel, Switzerland. *Geophysical Journal*  
750 *International*, 201(2), 1022-1039.
- 751 Festa, G., Adinolfi, G. M., Caruso, A., Colombelli, S., De Landro, G., Elia, L., ... & Zollo, A.  
752 (2021). Insights into mechanical properties of the 1980 Irpinia fault system from the analysis of a  
753 seismic sequence. *Geosciences*, 11(1), 28.
- 754 Gualandi, A., Nichele, C., Serpelloni, E., Chiaraluce, L., Anderlini, L., Latorre, D., ... & Avouac,  
755 J. P. (2017). Aseismic deformation associated with an earthquake swarm in the northern Apennines  
756 (Italy). *Geophysical Research Letters*, 44(15), 7706-7714.
- 757 Gulia, L., & Wiemer, S. (2019). Real-time discrimination of earthquake foreshocks and  
758 aftershocks. *Nature*, 574(7777), 193-199.
- 759 Hawthorne, J. C., & Bartlow, N. M. (2018). Observing and modeling the spectrum of a slow slip  
760 event. *Journal of Geophysical Research: Solid Earth*, 123(5), 4243-4265.

- 761 Herrmann, M., & Marzocchi, W. (2021). Inconsistencies and lurking pitfalls in the magnitude–  
762 frequency distribution of high-resolution earthquake catalogs. *Seismological Research*  
763 *Letters*, 92(2A), 909-922.
- 764 Herrmann, M., Piegari, E., & Marzocchi, W. (2022). Revealing the spatiotemporal complexity of  
765 the magnitude distribution and b-value during an earthquake sequence. *Nature*  
766 *Communications*, 13(1), 5087.
- 767 Hunter, J. D. (2007). Matplotlib: A 2D graphics environment. *Computing in science &*  
768 *engineering*, 9(03), 90-95. [Software]
- 769 Iannaccone, G., Zollo, A., Elia, L., Convertito, V., Satriano, C., Martino, C., Festa, G., Lancieri,  
770 M., Bobbio, A., Stabile, T. A., Vassallo, M. & Emolo, A., 2010. A prototype system for earthquake  
771 early-warning and alert management in southern Italy. *Bull. Earthq. Eng.*, 8(5), 11051129.
- 772 Improta, L., De Gori, P., & Chiarabba, C. (2014). New insights into crustal structure, Cenozoic  
773 magmatism, CO<sub>2</sub> degassing, and seismogenesis in the southern Apennines and Irpinia region from  
774 local earthquake tomography. *Journal of Geophysical Research: Solid Earth*, 119(11), 8283-8311.
- 775 Kaviris, G., Elias, P., Kapetanidis, V., Serpetsidaki, A., Karakonstantis, A., Plicka, V., ... &  
776 Bernard, P. (2021). The western Gulf of Corinth (Greece) 2020–2021 seismic crisis and cascading  
777 events: First results from the Corinth Rift Laboratory Network. *The Seismic Record*, 1(2), 85-95.
- 778 Keilis-Borok, V. (1959). On estimation of the displacement in an earthquake source and of source  
779 dimensions. *Annali di geofisica*, 12(2), 205-214.
- 780 Liu, F., Xue, S., Wu, J., Zhou, C., Hu, W., Paris, C., ... & Yu, P. S. (2020). Deep learning for  
781 community detection: progress, challenges and opportunities. *arXiv preprint arXiv:2005.08225*.
- 782 Lomax, A., Virieux, J., Volant, P., & Berge-Thierry, C. (2000). Probabilistic earthquake location  
783 in 3D and layered models: Introduction of a Metropolis-Gibbs method and comparison with linear  
784 locations. *Advances in seismic event location*, 101-134.
- 785 Lomax, A. (2020). Absolute location of 2019 Ridgecrest seismicity reveals a shallow Mw 7.1  
786 hypocenter, migrating and pulsing Mw 7.1 foreshocks, and duplex Mw 6.4 ruptures. *Bulletin of*  
787 *the Seismological Society of America*, 110(4), 1845-1858.
- 788 Madariaga, R. (1976). Dynamics of an expanding circular fault. *Bulletin of the Seismological*  
789 *Society of America*, 66(3), 639-666.

- 790 Mancini, S., Segou, M., Werner, M. J., Parsons, T., Beroza, G., & Chiaraluce, L. (2022). On the  
791 Use of High-Resolution and Deep-Learning Seismic Catalogs for Short-Term Earthquake  
792 Forecasts: Potential Benefits and Current Limitations. *Journal of Geophysical Research: Solid*  
793 *Earth*, *127*(11), e2022JB025202.
- 794 Marshall, S. T., & Morris, A. C. (2012). Mechanics, slip behavior, and seismic potential of  
795 corrugated dip-slip faults. *Journal of Geophysical Research: Solid Earth*, *117*(B3).
- 796 Marzocchi, W., Spassiani, I., Stallone, A., & Taroni, M. (2020). How to be fooled searching for  
797 significant variations of the b-value. *Geophysical Journal International*, *220*(3), 1845-1856.
- 798 Matrullo, E., De Matteis, R., Satriano, C., Amoroso, O., & Zollo, A. (2013). An improved 1-D  
799 seismic velocity model for seismological studies in the Campania–Lucania region (Southern  
800 Italy). *Geophysical Journal International*, *195*(1), 460-473.
- 801 Michele, M., Chiaraluce, L., Di Stefano, R., & Waldhauser, F. (2020). Fine-scale structure of the  
802 2016–2017 Central Italy seismic sequence from data recorded at the Italian National  
803 Network. *Journal of Geophysical Research: Solid Earth*, *125*(4), e2019JB018440.
- 804 Mori, J., & Frankel, A. (1990). Source parameters for small events associated with the 1986 North  
805 Palm Springs, California, earthquake determined using empirical Green functions. *Bulletin of the*  
806 *Seismological Society of America*, *80*(2), 278-295.
- 807 Mousavi, S. M., Ellsworth, W. L., Zhu, W., Chuang, L. Y., & Beroza, G. C. (2020). Earthquake  
808 transformer—an attentive deep-learning model for simultaneous earthquake detection and phase  
809 picking. *Nature communications*, *11*(1), 3952.
- 810 Münchmeyer, J., Woollam, J., Rietbrock, A., Tilmann, F., Lange, D., Bornstein, T., ... & Soto, H.  
811 (2022). Which picker fits my data? A quantitative evaluation of deep learning based seismic  
812 pickers. *Journal of Geophysical Research: Solid Earth*, *127*(1), e2021JB023499.
- 813 Okada, Y.(1992) Internal deformation due to shear and tensile faults in a half-space. *Bulletin of*  
814 *the Seismological Society of America*, *82* (2), 1018–1040.  
815 <https://doi.org/10.1785/BSSA0820021018>
- 816 Oth, A., Wenzel, F., & Radulian, M. (2007). Source parameters of intermediate-depth Vrancea  
817 (Romania) earthquakes from empirical Green's functions modeling. *Tectonophysics*, *438*(1-4), 33-  
818 56.

- 819 Palo, M., Picozzi, M., De Landro, G., & Zollo, A. (2023). Microseismicity clustering and mechanic  
820 properties reveal fault segmentation in southern Italy. *Tectonophysics*, 856, 229849.
- 821 Park, Y., Mousavi, S. M., Zhu, W., Ellsworth, W. L., & Beroza, G. C. (2020). Machine-learning-  
822 based analysis of the Guy-Greenbrier, Arkansas earthquakes: A tale of two  
823 sequences. *Geophysical Research Letters*, 47(6), e2020GL087032.
- 824 Park, Y., Beroza, G. C., & Ellsworth, W. L. (2022). Basement fault activation before larger  
825 earthquakes in Oklahoma and Kansas. *The Seismic Record*, 2(3), 197-206.
- 826 Park, Y., Beroza, G. C., & Ellsworth, W. L. (2023). A mitigation strategy for the prediction  
827 inconsistency of neural phase pickers. *Seismological Society of America*, 94(3), 1603-1612.
- 828 Picozzi, M., Bindi, D., Festa, G., Cotton, F., Scala, A., & D'Agostino, N. (2022). Spatiotemporal  
829 evolution of microseismicity seismic source properties at the Irpinia Near-Fault Observatory,  
830 Southern Italy. *Bulletin of the Seismological Society of America*, 112(1), 226-242.
- 831 Poupinet, G., Ellsworth, W. L., & Frechet, J. (1984). Monitoring velocity variations in the crust  
832 using earthquake doublets: An application to the Calaveras Fault, California. *Journal of*  
833 *Geophysical Research: Solid Earth*, 89(B7), 5719-5731.
- 834 Prieto, G. A., Shearer, P. M., Vernon, F. L., & Kilb, D. (2004). Earthquake source scaling and self-  
835 similarity estimation from stacking P and S spectra. *Journal of Geophysical Research: Solid*  
836 *Earth*, 109(B8).
- 837 Resor, P. G., & Meer, V. E. (2009). Slip heterogeneity on a corrugated fault. *Earth and Planetary*  
838 *Science Letters*, 288(3-4), 483-491.
- 839 Ross, Z. E., Trugman, D. T., Hauksson, E., & Shearer, P. M. (2019). Searching for hidden  
840 earthquakes in Southern California. *Science*, 364(6442), 767-771.
- 841 Ross, Z. E., Cochran, E. S., Trugman, D. T., & Smith, J. D. (2020). 3D fault architecture controls  
842 the dynamism of earthquake swarms. *Science*, 368(6497), 1357-1361.
- 843 Rovida, A. N., Locati, M., Camassi, R. D., Lolli, B., & Gasperini, P. (2019). Catalogo parametrico  
844 dei terremoti italiani cpti15, versione 2.0.
- 845 Rubin, A. M., Gillard, D., & Got, J. L. (1999). Streaks of microearthquakes along creeping  
846 faults. *Nature*, 400(6745), 635-641.

- 847 Rubinstein, J. L., & Beroza, G. C. (2007). Full waveform earthquake location: Application to  
848 seismic streaks on the Calaveras fault, California. *Journal of Geophysical Research: Solid*  
849 *Earth*, *112*(B5).
- 850 Sagy, A., Brodsky, E. E., & Axen, G. J. (2007). Evolution of fault-surface roughness with  
851 slip. *Geology*, *35*(3), 283-286.
- 852 Schaff, D. P., Bokelmann, G. H., Ellsworth, W. L., Zanker, E., Waldhauser, F., & Beroza, G.  
853 C. (2004). Optimizing correlation techniques for improved earthquake location. *Bulletin of the*  
854 *Seismological Society of America*, *94*(2), 705-721.
- 855 Scholz, C. H. (2015). On the stress dependence of the earthquake b value. *Geophysical Research*  
856 *Letters*, *42*(5), 1399-1402.
- 857 Scotto di Uccio, F., Scala, A., Festa, G., Picozzi, M., & Beroza, G. C. (2023). Comparing and  
858 integrating artificial intelligence and similarity search detection techniques: application to seismic  
859 sequences in Southern Italy. *Geophysical Journal International*, *233*(2), 861-874.
- 860 Scotto di Uccio, F., & Festa, G. (2023). Catalog of relocated seismic sequences in Irpinia [Data  
861 set]. Zenodo. <https://doi.org/10.5281/zenodo.10441456>
- 862 Shearer, P. M. (2002). Parallel fault strands at 9-km depth resolved on the Imperial fault, southern  
863 California. *Geophysical Research Letters*, *29*(14), 19-1.
- 864 Silverii, F., D'Agostino, N., Borsa, A. A., Calcaterra, S., Gambino, P., Giuliani, R., & Mattone, M.  
865 (2019). Transient crustal deformation from karst aquifers hydrology in the Apennines  
866 (Italy). *Earth and Planetary Science Letters*, *506*, 23-37.
- 867 Simon, V., Kraft, T., Diehl, T., & Tormann, T. (2021). Possible Precursory Slow-Slip to Two ML ~  
868 3 Main events of the Diemtigen Microearthquake Sequence, Switzerland. *Geophysical Research*  
869 *Letters*, *48*(19), e2021GL093783.
- 870 Spallarossa, D., Cattaneo, M., Scafidi, D., Michele, M., Chiaraluce, L., Segou, M., & Main, I. G.  
871 (2021). An automatically generated high-resolution earthquake catalog for the 2016–2017 Central  
872 Italy seismic sequence, including P and S phase arrival times. *Geophysical Journal*  
873 *International*, *225*(1), 555-571.
- 874 Stabile, T. A., Satriano, C., Orefice, A., Festa, G., & Zollo, A. (2012). Anatomy of a  
875 microearthquake sequence on an active normal fault. *Scientific reports*, *2*(1), 410.

- 876 Stucchi, M., Meletti, C., Montaldo, V., Crowley, H., Calvi, G. M., & Boschi, E. (2011). Seismic  
877 hazard assessment (2003–2009) for the Italian building code. *Bulletin of the Seismological Society*  
878 *of America*, *101*(4), 1885-1911.
- 879 Sukan, M., Campanella, S., Chiaraluce, L., Michele, M., & Vuan, A. (2023). The unlocking  
880 process leading to the 2016 Central Italy seismic sequence. *Geophysical Research Letters*, *50*(5),  
881 e2022GL101838.
- 882 Supino, M., Festa, G., & Zollo, A. (2019). A probabilistic method for the estimation of earthquake  
883 source parameters from spectral inversion: application to the 2016–2017 Central Italy seismic  
884 sequence. *Geophysical Journal International*, *218*(2), 988-1007.
- 885 Supino, M., Poiata, N., Festa, G., Vilotte, J. P., Satriano, C., & Obara, K. (2020). Self-similarity  
886 of low-frequency earthquakes. *Scientific Reports*, *10*(1), 6523.
- 887 Tan, Y. J., Waldhauser, F., Ellsworth, W. L., Zhang, M., Zhu, W., Michele, M., ... & Segou, M.  
888 (2021). Machine-learning-based high-resolution earthquake catalog reveals how complex fault  
889 structures were activated during the 2016–2017 Central Italy sequence. *The Seismic Record*, *1*(1),  
890 11-19.
- 891 Trugman, D. T., & Shearer, P. M. (2017). GrowClust: A hierarchical clustering algorithm for  
892 relative earthquake relocation, with application to the Spanish Springs and Sheldon, Nevada,  
893 earthquake sequences. *Seismological Research Letters*, *88*(2A), 379-391.
- 894 Uieda, L., Tian, D., Leong, W. J., Toney, L., Schlitzer, W., Yao, J., Grund, M., Jones, M., 646  
895 Materna, K., Newton, T., Ziebarth, M., & Wessel, P. (2021). PyGMT: A Python 647 interface for  
896 the Generic Mapping Tools (v0.3.1) [Software]
- 897 Vassallo, M., Festa, G., Bobbio, A., & Serra, M. (2016). Low shear velocity in a normal fault  
898 system imaged by ambient noise cross correlation: The case of the Irpinia fault zone, Southern  
899 Italy. *Journal of Geophysical Research: Solid Earth*, *121*(6), 4290-4305.
- 900 Vuan, A., Sukan, M., Amati, G., & Kato, A. (2018). Improving the detection of low-magnitude  
901 seismicity preceding the Mw 6.3 L'Aquila earthquake: Development of a scalable code based on  
902 the cross correlation of template earthquakes. *Bulletin of the Seismological Society of*  
903 *America*, *108*(1), 471-480.

- 904 Vuan, A., Brondi, P., Sugan, M., Chiaraluce, L., Di Stefano, R., & Michele, M. (2020). Intermittent  
905 slip along the Alto Tiberina low-angle normal fault in central Italy. *Geophysical Research*  
906 *Letters*, *47*(17), e2020GL089039.
- 907 Waldhauser, F., & Ellsworth, W. L. (2000). A double-difference earthquake location algorithm:  
908 Method and application to the northern Hayward fault, California. *Bulletin of the seismological*  
909 *society of America*, *90*(6), 1353-1368.
- 910 Waldhauser, F. (2001). hypoDD--A program to compute double-difference hypocenter locations.
- 911 Waldhauser, F., Michele, M., Chiaraluce, L., Di Stefano, R., & Schaff, D. P. (2021). Fault planes,  
912 fault zone structure and detachment fragmentation resolved with high-precision aftershock  
913 locations of the 2016–2017 central Italy sequence. *Geophysical Research Letters*, *48*(16),  
914 e2021GL092918.
- 915 Westaway, R., & Jackson, J. (1987). The earthquake of 1980 November 23 in Campania—  
916 Basilicata (southern Italy). *Geophysical Journal International*, *90*(2), 375-443.
- 917 Yoon, C. E., Yoshimitsu, N., Ellsworth, W. L., & Beroza, G. C. (2019). Foreshocks and mainshock  
918 nucleation of the 1999 M w 7.1 Hector Mine, California, Earthquake. *Journal of Geophysical*  
919 *Research: Solid Earth*, *124*(2), 1569-1582.
- 920 Zhu, W., & Beroza, G. C. (2019). PhaseNet: A deep-neural-network-based seismic arrival-time  
921 picking method. *Geophysical Journal International*, *216*(1), 261-273.
- 922 Zollo, A., Orefice, A., & Convertito, V. (2014). Source parameter scaling and radiation efficiency  
923 of microearthquakes along the Irpinia fault zone in southern Apennines, Italy. *Journal of*  
924 *Geophysical Research: Solid Earth*, *119*(4), 3256-3275.

Supporting Information for

## **Characterization and evolution of seismic sequences in the normal fault environment of the Southern Apennines**

*Francesco Scotto di Uccio*<sup>1</sup>, *Maddalena Michele*<sup>2</sup>, *Claudio Strumia*<sup>1</sup>, *Mariano Supino*<sup>2</sup>,  
*Gregory C. Beroza*<sup>3</sup>, *Lauro Chiaraluce*<sup>2</sup>, *Nicola D'Agostino*<sup>2</sup>, *Gaetano Festa*<sup>1,2</sup>

<sup>1</sup> Department of Physics 'Ettore Pancini', University of Napoli Federico II, 80126 Napoli, Italy.

<sup>2</sup> Istituto Nazionale di Geofisica e Vulcanologia, Rome, Italy.

<sup>3</sup> Department of Geophysics, Stanford University, Stanford, CA 94305, USA.

Corresponding author: Francesco Scotto di Uccio ([francesco.scottodiuccio@unina.it](mailto:francesco.scottodiuccio@unina.it))

### **Contents of this file**

Table S1

Figure S1, S2, S3

### **Introduction**

In the Supporting Information we report the sequence labelling using in this study with respect to the sequence indexing in Scotto di Uccio et al. (2023) (Table S1), the velocity models that have been tested for earthquake location (Figure S1), the waveforms from two events belonging to the two clusters identified from the Rocca San Felice seismic sequence (Figure S2) and the results for the spectral inversion using different attenuation factors (Figure S3)

Sequence location	$M_{l_{main}}$	IDX in this study	IDX in Scotto di Uccio et al. (2023)
Lioni (AV)	2.7	1	2
San Gregorio Magno (SA)	2.8	2	3
Lioni (AV)	3.7	3	4
Laceno (AV)	1.8	4	5
Ricigliano (SA)	3.0	5	6
Lioni (AV)	2.8	6	8
Bella (PZ)	3.1	7	10
Rocca San Felice (AV)	3.0	8	1

**Table S1:** Sequence labelling using in this study with respect to the indexing in Scotto di Uccio et al. (2023)

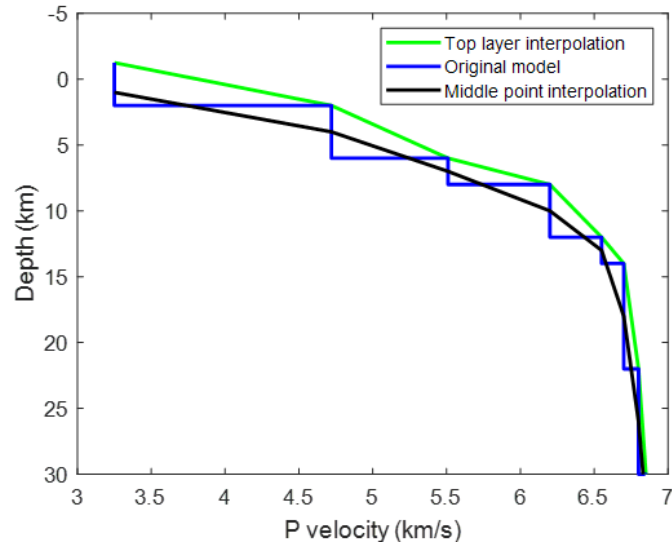


**Figure S1:** P wave velocity models tested for earthquake location. Starting from the 1D layered velocity model (blue line, Matrullo et al. 2013) we derived two gradient models, which smooth the discontinuities in the wave velocity across layer boundaries, by linearly interpolating values between either the top (green line) or the middle points (black line) of the layers.

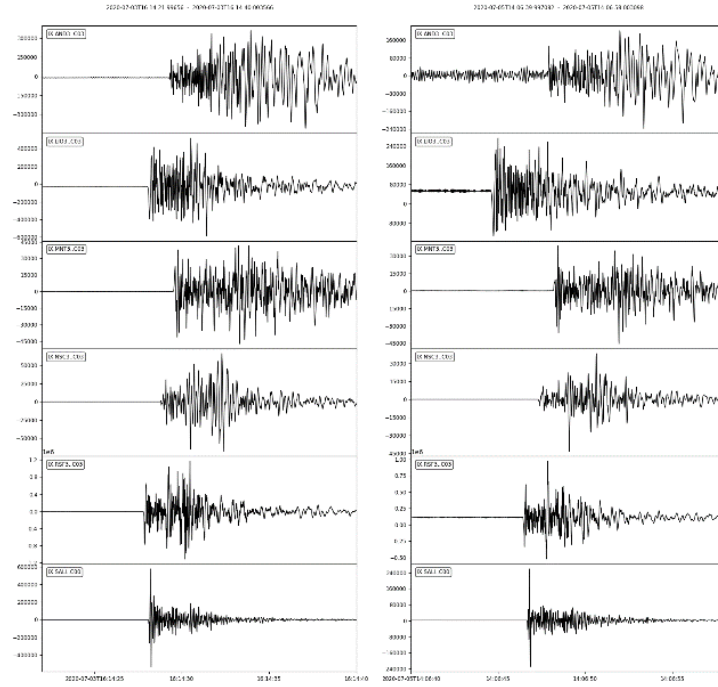


**Figure S2:** Vertical component of ground motion records (velocity for stations AND3, LIO3, MNT3, NSC3, RSF3, acceleration for station SALI) for two events belonging to the two clusters identified in the Rocca San Felice seismic sequence (IDX 8). Traces are bandpass filtered between [1 – 20] Hz. The two events differ for the station recording the first P-wave arrival: for the event belonging to the first cluster (left panel) the first P-wave arrival is observed at RSF3 while for the second cluster (right panel) the first P-wave arrival is recorded at LIO3.

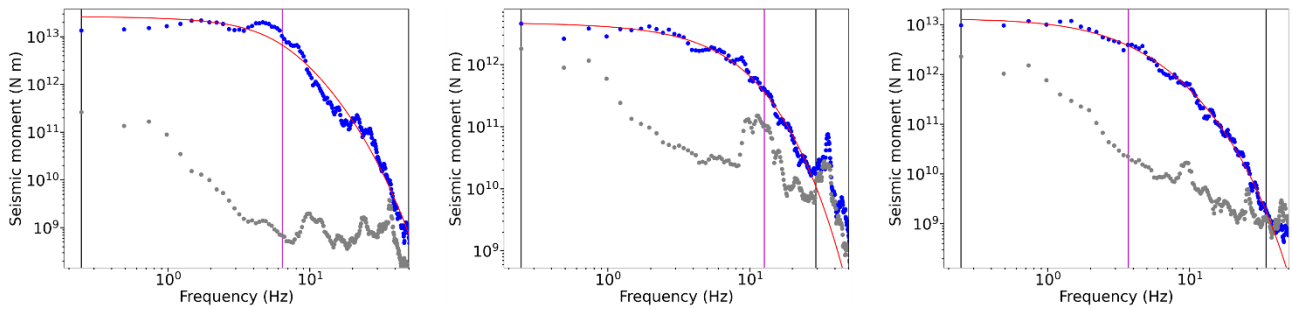


**Figure S3:** Spectral inversion of a  $M_1 = 2.8$  earthquake using different attenuation factors for the stations. Left panel: inversion using  $Q_{EGF}$  at NSC3 station. Central panel: inversion using  $Q_{LOC}$  at SCL3 station. Right panel: inversion using  $Q_{REG}$  at VDS3.